Geometry and Evolution of Wrench Tectonics in the NE Lau Basin

M. O. Anderson[1], C. Norris-Julseth[1], K. H. Rubin[2], K. Haase[3], M. D. Hannington[4,5], A.T. Baxter[4], and M. S. Stewart[4†]

[1]Department of Earth Sciences, University of Toronto, 22 Russell Street, Toronto, Ontario, M5S 3B1, Canada

[2]Department of Geology and Geophysics, SOEST, University of Hawaii, 1680 East-West Road, Honolulu, Hawaii, 96822, USA

[3]GeoZentrum Nordbayern, Friedrich-Alexander University of Erlangen-Nürnberg, Schlossgarten 5, D-91054 Erlangen, Germany

[4]Department of Earth Sciences, University of Ottawa, 25 Templeton, Ottawa, Ontario, K1N 6N5, Canada

[5]GEOMAR, Helmholtz Centre for Ocean Research Kiel, Wischhofstrasse 1-3, 24148 Kiel, Germany

Corresponding author: Melissa O. Anderson (melissao.anderson@utoronto.ca)

[†]Current address: Department of Earth and Environmental Sciences, Mount Royal University, 4825 Mount Royal Gate SW, Calgary, Alberta, T3E 6K5, Canada

Key Points:

- NE Lau basin is dominated by strike-slip kinematics associated with reactivation of pre-existing extensional faults
- Seamount collision segmented the forearc and induced a counter-clockwise rotation of the stress field in the back-arc
- Riedel shearing promotes distributed rear-arc volcanism, in contrast to typical ridge-centered back-arc volcanism

Abstract

The transition from subduction to transform motion along horizontal terminations of trenches is associated with tearing of the subducting slab and wrench tectonics in the overriding plate. One prominent example is the northern Tonga subduction zone, where the influence of wrench tectonics is indicated by abundant strike-slip faulting in the NE Lau back-arc basin. We explore the back-arc dynamics of this region for the first time through structural lineament analyses and kinematic analyses interpreted from ship-based multibeam bathymetry and Centroid-Moment Tensor data. Our results indicate two distinct sets of Riedel shear structures that are associated with a counter-clockwise rotation in the stress field. We propose that this rotation is driven by the collision of the previously unstudied Capricorn Seamount(s). The strain of this collision was accommodated by right-lateral slip along the adjacent crustal scale fault, known as the Fonualei Discontinuity, which segmented the fore-arc. Internal deformation of the northern tectonic block may have been enhanced by friction along the northern boundary imparting westward-directed stress. This study highlights the importance of non-rigid plate kinematics and extensive re-activation of pre-existing faults in this region. Importantly, these structures directly control the development of complex volcanic-compositional provinces, which are characterized by variably-oriented spreading centers, off-axis volcanic ridges, extensive lava flows, and point-source rear-arc volcanoes that sample a heterogenous mantle wedge, with sharp gradients and contrasts in composition and magmatic affinity. This study adds to our understanding of the influence of subduction-transform motions and terrane collisions on the structural and magmatic evolution of back-arcs.

Keywords

NE Lau Basin; back-arc; wrench tectonics; seamount collision; Riedel shear; bathymetry

1. Introduction

Back-arc basins are extensional features formed behind subduction zones by progressive rifting of volcanic arcs until passive mantle upwelling creates new oceanic crust (Karig, 1970). Their initiation is triggered by either processes of hinge-rollback (Chase, 1978; Scholz & Campos, 1995), and/or slab anchoring on the trenchward side of the upper plate (Heuret & Lallemand, 2005). Once back-arc spreading is established, it may continue regardless of the motion of the overriding plate (Sdrolias & Müller, 2006). Movement of the overriding plate relative to the arc and subduction zone leads to a diverse arrangement of plates and deformation styles within the near-arc and back-arc environments (Heuret & Lallemand, 2005).

The process of hinge-rollback is often disrupted by terrane collisions, where topographic features on the subducting plate, such as seamounts or oceanic plateaus, can cause a subduction zone to become temporarily "clogged" or permanently "locked" due to compressional forces on the arc exerted by the seamount (e.g., Ruellan et al., 2003; Anderson et al., 2016; Mallard et al., 2016). This in turn may induce oblique subduction and strike-slip tectonics at the edge of the overriding plate (Ruellan et al., 2003). This can alter the stress field causing plates to rearrange, triggering rift propagation and the creation of new microplate boundaries in the back-arc (Hey et al., 1995; Wallace et al., 2005; Zellmer & Taylor, 2001). Edge-driven kinematics are common along the boundaries of microplates, where microplate rotation is driven by the motion of the two larger plates the microplate is pinched between (Schouten et al., 1993). These microplate rotations can cause block rotations, shearing, and further rift propagation (e.g., Easter Microplate: Neves et al., 2003).

Hinge-rollback, seamount subduction, microplate interactions, and variations in trench geometry and/or subduction angle all influence the state of stress in the overriding plate, driving

upper mantle flow and magmatic upwelling, and the formation of structures that provide pathways for magma to reach the surface. This paper focuses on the recent kinematic evolution of the NE Lau Basin, which is one of the most volcanically- and tectonically-active places on Earth (Embley et al., 2009; Rubin et al., 2013; Embley & Rubin, 2018). A combination of remote-predictive geological and structural maps based on high-resolution multibeam bathymetry collected by the *R/V Falkor* expedition FK171110 in 2017 and *R/V Sonne* expedition SO-263 in 2018, compiled with previously-collected bathymetry, are used to interpret the volcanic and structural evolution of the area, providing insight into geodynamic controls on back-arc development.

2. Tectonic Setting

The Tonga-Kermadec subduction zone in the western Pacific extends over 2000 km from New Zealand to Fiji, where the Pacific Plate subducts westward beneath the Indo-Australian Plate (**Fig. 1**). The subduction zone is segmented into the Tonga Trench north of 26°S (associated with the Tofua segment of the Tonga arc) and the Kermadec Trench to the south. Subduction rates along the northern Tonga Trench are the fastest on Earth, with rates of up to 240 mm yr^{-1} sustained for the past 0.78 m.y. (Bevis et al., 1995; Zellmer & Taylor, 2001). There is a southward decrease in subduction rates to 60 mm yr^{-1}, associated with increasing convergence angle obliquity (Bevis et al., 1995). The subducting slab dips uniformly and steeply at about 50° until it meets the northern termination of the subduction zone where it dips more shallowly (Millen & Hamburger, 1998; Hall & Spakman, 2002). Here, a sharp bend to a westerly-direction is associated with a transition from subduction to transform motion, forming a Subduction-Transform-Edge-Propagator (STEP) boundary (Govers & Wortel, 2005).

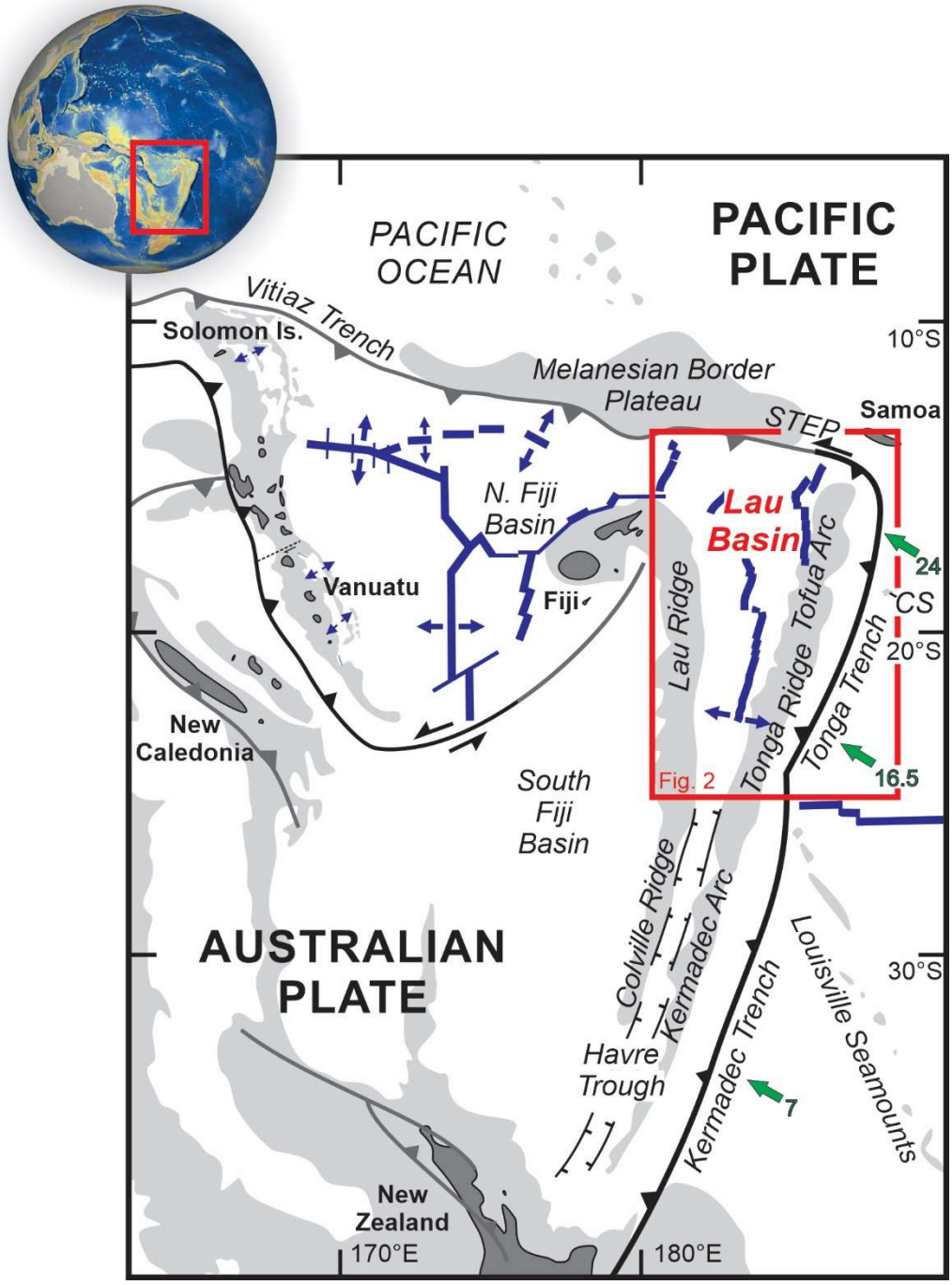

Figure 1. Geographic location and tectonic features of the southwest Pacific modified from Hall (2002). Light grey areas represent the 2000 m isobaths, green arrows indicate convergence directions and rates (cm y^{-1}) from Bevis et al. (1995), and blue lines represent spreading centers. CS = Capricorn Seamount(s), STEP = Subduction-Transform-Edge-Propagator boundary.

This boundary is associated with vertical tearing that causes a piece of the subducting plate to remain at surface (Nijholt & Govers, 2015).

Rifting of the northern volcanic arc at 5.5–6 Ma formed the Lau Basin (**Fig. 2**), which evolved to mature seafloor spreading at ca. 5 Ma (Wiedicke & Collier, 1993; Taylor et al., 1996). As the Tonga Trench migrated eastward, arc volcanism shifted from the remnant Lau Ridge to form the new Tofua Arc at 3.5 Ma (Tappin et al., 1994). In the southern part of the subduction zone, rifting of the Kermadec Arc at ca. <2 Ma produced the Havre Trough (Wysoczanski et al., 2019). Unlike the Lau Basin to the north, the Havre Trough is not thought to be undergoing passive mantle upwelling and mature seafloor spreading (e.g., Todd et al., 2010; Tontini et al., 2019).

The modern Lau Basin displays a tapering V-shape with a width of ~500 km in the north, narrowing to 200 km in the south where it merges with the Havre Trough (**Fig. 2**). There is a trend of increasing tectonic complexity northward in the Lau Basin (Sleeper & Martinez, 2016). In the south, two plates (Tongan and Australian) are separated by a single segmented spreading center. In the north, the Niuafo'ou Microplate has been interpreted to occur between the Tongan and Australian plates, although it is bounded by and contains numerous small spreading centers and propagating rifts, and so structurally might be even more complex (i.e., multiple microplates). There are likely several other micro- or nano-plates in the northern basin with poorly-defined (possibly diffuse) boundaries that have not been studied in detail (Zellmer & Taylor, 2001; Phillips, 2003; Conder & Wiens, 2011). The formation of microplates may be related to processes involving ultrafast opening rates, northward extension, or edge-driven kinematics along the STEP boundary (Conder & Wiens, 2011; Sleeper & Martinez, 2016). Plate reconstructions by Sleeper and Martinez (2016) suggest that non-rigid plate behavior may

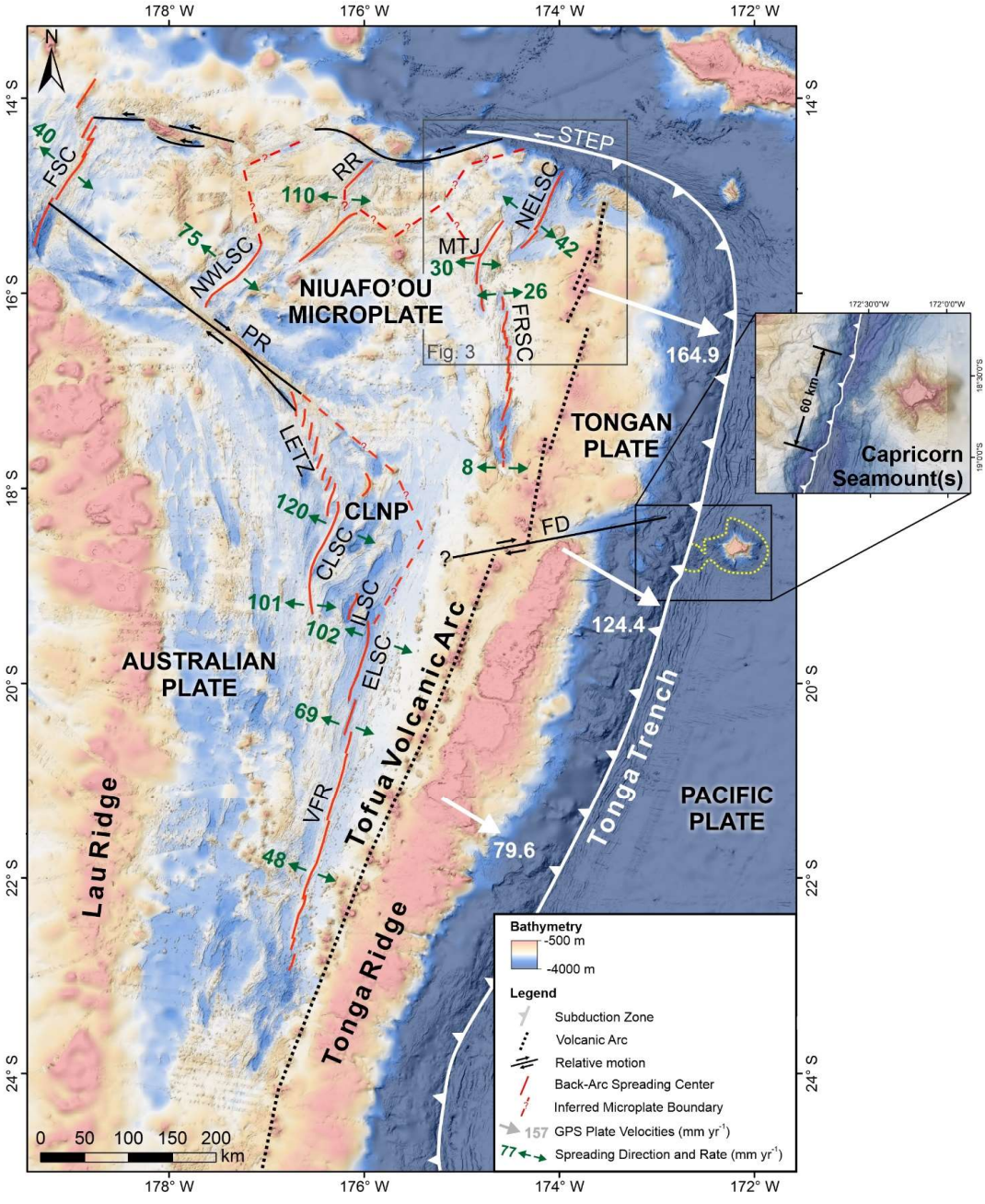

Figure 2. Tectonic features and regional bathymetry of the NE Lau Basin compiled from Rubin et al. (2010; 2018), Martinez et al. (2013), Haase et al. (2018) and GEBCO compilation group (2019). Inferred microplate boundaries based on seismicity from Conder and Wiens (2011), GPS velocities of Tonga relative to Australia from Phillips (2003) and spreading directions and rates (mm yr^{-1}) for the FSC from Pelletier et al. (2001), for the NWLSC and RR from Lupton et al. (2015) following Bird (2003), and for the CLSC, ELSC, FRSC, LETZ, MTJ, NELSC, and VFR from Sleeper and Martinez (2016). CLNP = Central Lau Nano-Plate; CLSC = Central Lau Spreading Center; ELSC = Eastern Lau Spreading Center; FD = Fonualei Discontinuity; FRSC = Fonualei Rift and Spreading Center; FSC = Futuna Spreading Center; ILSC = Intermediate Lau Spreading Center; LETZ = Lau Extensional Transform Zone; MTJ = Mangatolu Triple Junction; NELSC = North-East Lau Spreading Center; NWSC = North-West Lau Spreading Center; PR = Peggy Ridge; RR = Rochambeau Rifts; VFR = Valu Fa Ridge.

be important in this area, where plate boundaries can propagate and rotate, and experience intraplate deformation.

South of the NE Lau Basin study area, seamount subduction also plays an important role in tectonic evolution of the arc and back-arc. The Louisville Seamount Chain (LSC) is colliding with the subduction zone at 26°S, inducing compression and rotation of the volcanic arc, and effectively stalling subduction and back-arc spreading in the southern basin (**Fig. 1**; Ruellan et al., 2003; Wallace et al., 2004; Stratford et al., 2015). At 18°30′S, a partially-subducted portion of the Capricorn Seamount (or seamounts) is indicated by irregular topography rising ~3800 m above the adjacent trench (**Fig. 2**). This collision zone has not been studied in depth but may have an effect similar to the LSC. Opposite the colliding seamount is an area of raised, flat-topped marine terraces in the forearc—a typical feature associated with seamount subduction—forming the Tonga Ridge. Immediately to the north of the collision zone is a large fault zone in the overriding plate called the Fonualei Discontinuity (FD), oriented at a high angle to the trench. This fault extends WSW from the fore-arc and offsets the arc by up to ~40 km. Previous authors suggest that the FD could be related to the initial collision zone with the LSC (e.g., Bonnardot et al., 2007), but the relationship with the collision of the Capricorn Seamount(s) has not yet been investigated. A second, smaller fault has been interpreted at 16°S, offsetting the arc by ~28 km (e.g., Baker et al., 2019); however, there is no surface expression of this fault and this offset may instead reflect the spacing of en echelon segments of the arc.

This dynamic tectonic setting results in several distinct attributes among modern-day intra-oceanic subduction zones, including the fastest convergence and back-arc opening rates (Bevis et al., 1995; Embley & Rubin, 2018), highest upper mantle temperatures (Conder & Wiens, 2006), one of Earth's coolest slab parameters and among the highest slab water fluxes

(van Keken et al., 2011). We explore the complex structural evolution of the NE Lau Basin—where these processes are the most pronounced—to understand the links between regional geodynamics, microplate tectonics, and magmatic-hydrothermal activity in this unique natural laboratory.

3. Methods

Ship-based multibeam bathymetric data from the NE Lau Basin were collected during two R/V Kilo Moana cruises in 2010 (KM1024; Rubin et al., 2010) and 2011 (KM1129; Martinez et al., 2013), and are supplemented here with new data from R/V Falkor cruise FK171110 in 2017 (Rubin et al., 2018), and R/V Sonne cruise SO-263 in 2018 (Tonga Rift: Haase et al., 2018). The R/V Kilo Moana and R/V Sonne are equipped with Kongsberg EM 122 multibeam echo sounders with operating frequencies of 12 kHz, and the R/V Falkor is equipped with a Kongsberg EM 302 multibeam echo sounder with an operating frequency of 30 kHz. The combined surveyed area is 40,760 km^2, covering 73% of the map area (**Fig. S1**). The raw data were cleaned and gridded at cell sizes of 30 to 50 m by the various shipboard scientific parties. The data were compiled together with the 2019 GEBCO grid (GEBCO Compilation Group, 2019) and reprocessed using the "Terrain Texture Shading" (TTS) technique developed by Brown (2014) as an interpretive tool in applied geomatics to reveal subtle surface and structural features that can be directly correlated with seafloor geomorphology (e.g., Augustin et al., 2016; Anderson et al. 2016; 2017).

The processed bathymetric maps are interpreted here together with acoustic backscatter data from SO-263 and FK171110 to create a new remote-predictive geological map of the NE Lau basin, following the criteria outlined by Anderson et al. (2016; 2017) and Klischies et al. (2019). Lithological data from ROV sampling, TV grabs (visually aided ship-based scoop

sampling), and wax coring from the SO-263 cruise and a compilation of data from literature was used to inform the geological maps (**Fig. S1**). In addition to lithological units, fully georeferenced measurements of structural features, including faults, volcanic ridges, and lineaments are interpreted and digitized. Relative ages of the mapped units were established from overlapping and cross-cutting relationships, and morphological and backscatter evidence of young volcanic flow features and sediment cover.

Further "ground-truthing" of the map legend was provided by seafloor observations during ROV dives; seventeen dives were with the MARUM ROV Quest 4000 during the 2018 SO-263 cruise, seven dives from the TN234 cruise using WHOI ROV Jason-2 (five dives at West Mata and two dives on the southern NELSC; Resing et al., 2009). The SO-263 QUEST 4000 dives included one that transected the wall of the graben in the NE map area that hosts the Niua volcano (Escarpment A), one that transected the northern Tonga forearc, six dives at vent sites at the Niua arc volcano, six dives at various locations around Niuatahi volcano, and two dives at the southern NELSC near the Maka seamount and its summit hydrothermal vent site (Haase et al., 2018).

Finally, fault kinematics were interpreted from offset features where cross-cutting relationships exist. This was supplemented by centroid-moment tensor (CMT) focal mechanisms from the Harvard CMT catalogue (www.globalcmt.org; Dziewonski et al., 1981; Ekström et al., 2012) for earthquakes with $M_W \geq 5$ and depths of ≤25 km. To determine the correct fault-plane solution, each CMT was interpreted in the context of the dominant lineament orientation (**Fig. S2**). The CMTs were classified according to type and orientation, following the classification of lineaments. Fault planes were plotted as stereonets to check for consistency in the groupings (**Fig. S3**). This technique has been used since scientists first started recording seismic moments

(e.g., Mckenzie, 1969) and has been recently applied to understanding changing stress regimes in the Lau Basin at a regional scale (Baxter et al., submitted).

4. Geological and structural features of the NE Lau Basin

Most of the prior work towards understanding the geology of the Lau Basin has been focused on the southern basin along the Eastern and Central Lau Spreading Centers, where crustal accretion resembles mid-ocean ridges. This contrasts the processes of crustal accretion in the NE Lau Basin, where a diffuse system of back-arc extension, short-lived rifts, spreading centers, jumping ridge crests, and point-source volcanism dominate (Taylor et al., 1996; Embley et al., 2009). We present new remote-predictive geological and structural maps of the NE Lau Basin (**Figs. 3** and **4**; **Table S1**), which highlight the wide variety of rock types, extensive volcanism, and complex structural fabrics resulting from the dynamic evolution of the area.

4.1. Rifts and spreading centers

The spreading centers in the study area include two of the three arms of the Mangatolou Triple Junction (MTJ; formerly the "Kings Triple Junction"), the North-East Lau Spreading Center (NELSC), and the northern half of the Fonualei Rift and Spreading Center (FRSC). The spreading centers primarily erupt basalt, with lesser amounts of basaltic andesite, andesite, rhyolite, and boninite, with distinct geochemical signatures along each spreading center (Falloon et al., 2007; Tian et al., 2011; Escrig et al., 2012; Rubin et al., 2018; Haase et al., 2018). Sampling of the MTJ has revealed a diverse suite of lithologies, spanning the compositional range from basalt to andesite to dacite (Nilsson et al., 1989; Falloon et al., 1992; Hawkins, 1995; Langmuir et al., 2006). The NELSC has a mixed geochemical signature of OIB and N-MORB, in addition to subtle arc-like affinities (Keller et al., 2008; Zhang et al., 2018). Along the southern MTJ arm and the FRSC, IAB signatures are most abundant, with boninitic

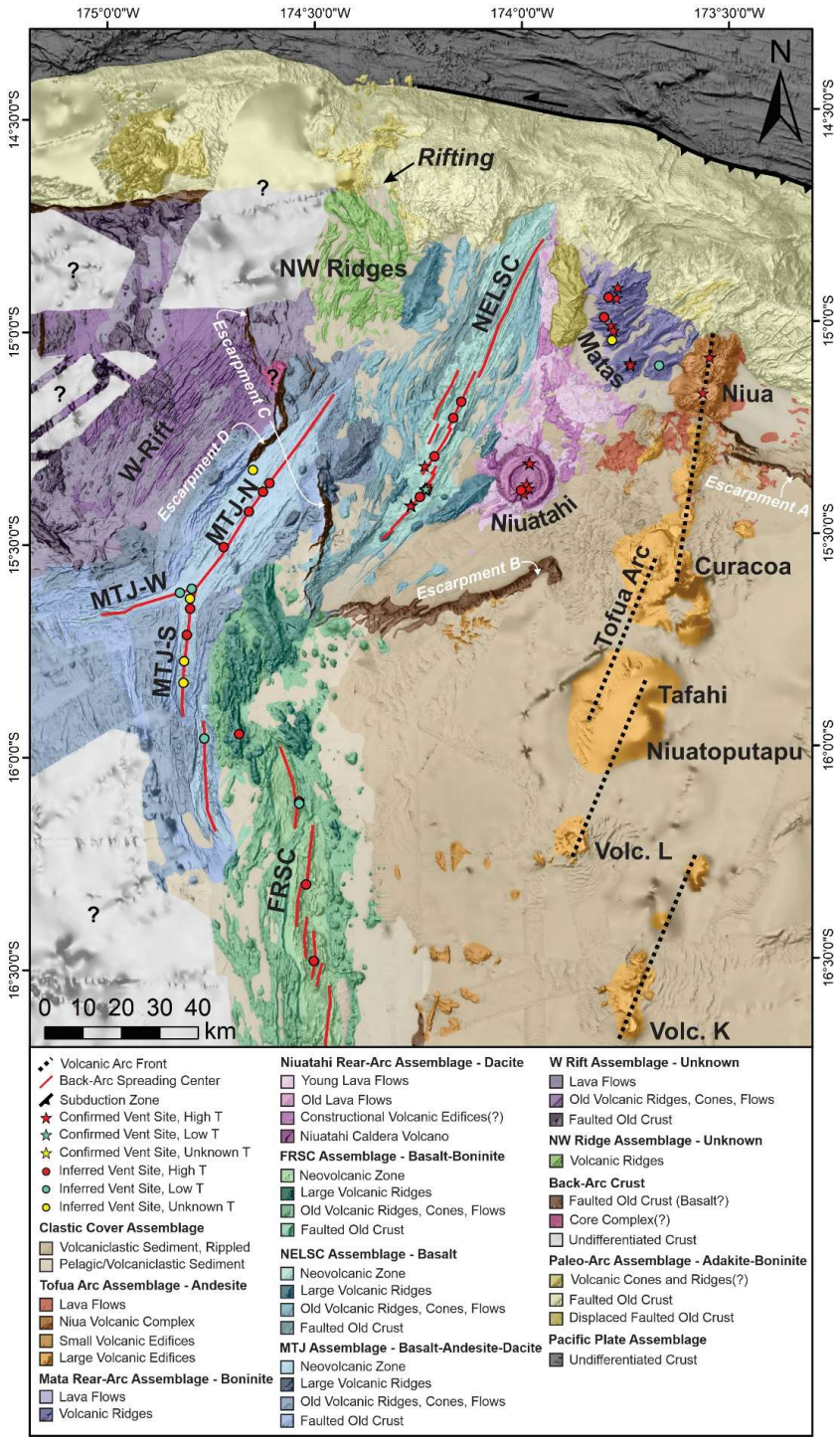

Figure 3. Remote-predicted geological map of the NE Lau basin interpreted from seafloor geomorphology and limited sampling (**Fig. S1**), overlain on a compilation of ship multibeam bathymetry (from Rubin et al., 2010; 2018; Martinez et al., 2013; Haase et al., 2018) and the GEBCO 2019 regional bathymetric grid (GEBCO compilation group, 2019). Hydrothermal vent sites compiled from the FK171111 and SO-263 cruises (Rubin et al., 2018; Haase et al., 2018), InterRidge Vents Database v. 3.4 (Beaulieu & Szafranski, 2019), and Baker et al. (2019). Abbreviations as in **Fig. 2**. Additional details on map units outlined in **Table S1**.

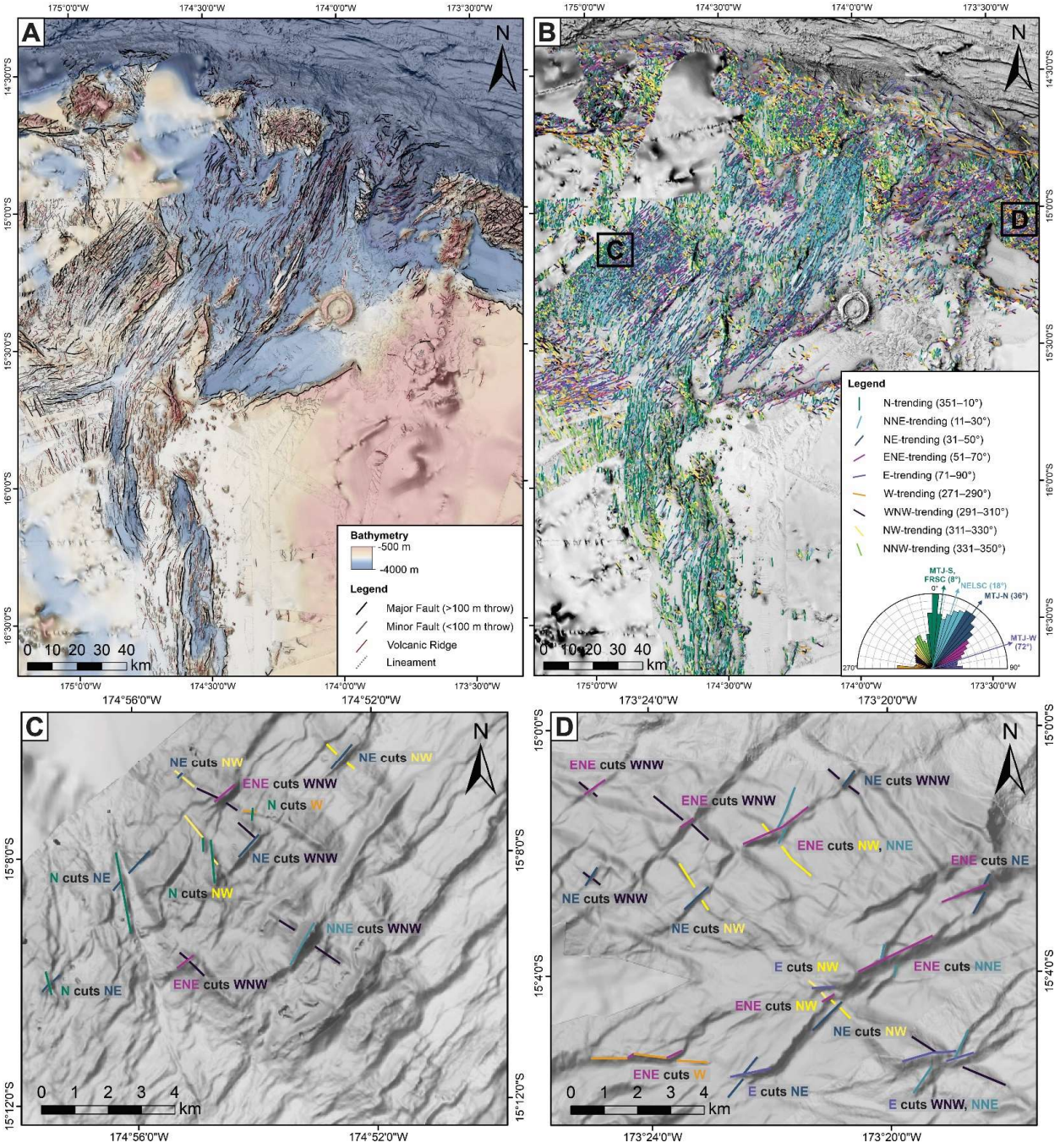

Figure 4. Interpreted structural lineaments in the NE Lau basin: (a) by type, and (b) by orientation. Close-ups showing examples of cross-cutting relationships of selected structures for: (c) the NW rift zone, and (d) the paleo-arc crust, summarized in **Table 1**. Abbreviations and bathymetric data sources as in **Fig. 2**.

signatures in the central FRSC associated with magmas captured from the volcanic front (Escrig et al., 2012). Despite the proximity of these spreading centers (~30 km), there is a distinct compositional change between them (e.g., Keller et al., 2008). Therefore, these spreading centers are mapped as separate geological assemblages, each consisting of several units (**Fig. 3**).

The MTJ is a ridge-ridge-ridge triple junction with each of the three spreading segments displaying distinct morphologies (**Fig. 3**). The MTJ assemblage consists of a neovolcanic zone along the center of each segment, flanked by older crust that is variably faulted or ridge-like. The western arm (MTJ-W) is oriented ENE, accommodating N-S extension in the basin, and is considered to be a failed rift (Phillips, 2003). This arm has a narrow neovolcanic zone (up to 3 km wide) within a flat axial valley and is heavily faulted, with structures that are oriented ENE to E-W (**Fig. 5d–e**). The southern arm (MTJ-S) consists of two spreading segments that are oriented N-S, with an axial valley containing a neovolcanic zone that is up to 5 km wide. This neovolcanic zone is dominated by sheet flows and small fissures. Distal volcanic ridges along the flanks of the MTJ-S extend up to 40 km to the west of the spreading center and are steeper and have more relief than ridges along the other arms. In the northern part of the MTJ-S arm, the ridges are cross-cut by E-W trending faults associated with the MTJ-W arm. The southern part of the MTJ-S arm is dominated by N-trending structures (**Fig. 5a**) with minor NNW-trending structures in the south (**Fig. 5i**). The northern MTJ arm (MTJ-N) is a single NNE- to NE-trending segment with a broad axial valley up to 18 km wide, which contains the neovolcanic zone and is bounded by steep faults. The northern and southern ends of the segment consist of small volcanic ridges up to ~180 m tall. The central part of the segment has higher relief with a broad shield-like morphology, and a subtle axial graben up to ~2 km wide. Intense off-axis volcanism occurs along a large ridge in the north (centered at 15°18′S, 174°25′W), which is up to

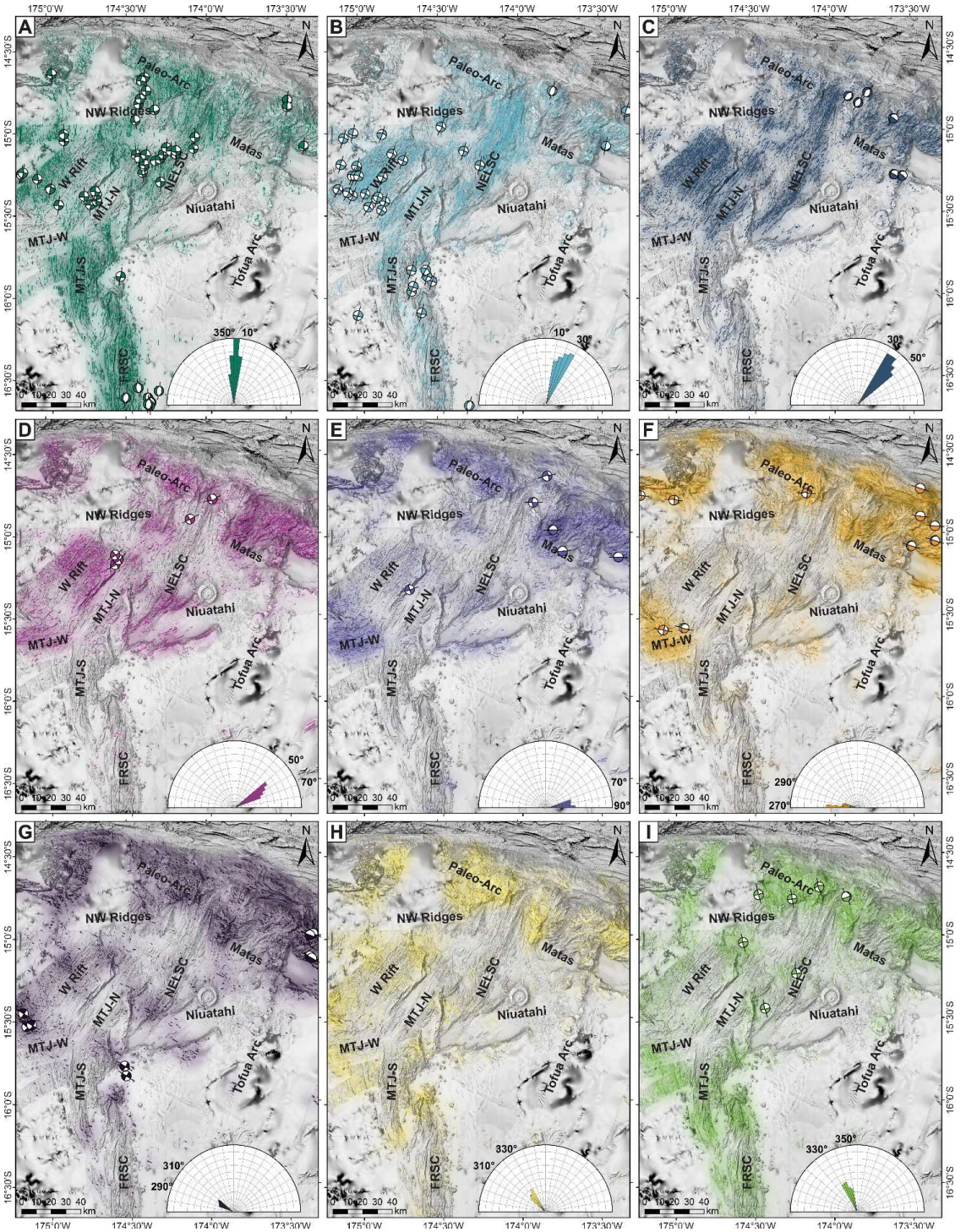

Figure 5. Interpreted structural lineaments, relative lineament densities (lineament km per km^2), and shallow (<25 km) CMT focal mechanisms from Harvard (www.globalcmt.org; Dziewonski et al., 1981; Ekström et al., 2012), classified according to interpreted strike: (a) N-trending (max. 0.57 km/km^2), (b) NNE-trending (max. 1.25 km/km^2), (c) NE-trending (max. 1.04 km/km^2), (d) ENE-trending (max. 0.64 km/km^2), (e) E-trending (max. 0.57 km/km^2), (f) W-trending (max. 0.24 km/km^2), (g) WNW-trending (max. 0.29 km/km^2), (h) NW-trending (max. 0.29 km/km^2), (i) NNW-trending (max. 0.33 km/km^2). Stereonets of CMTs grouped according to interpreted strike shown in **Fig. S3**.

1300 m tall and 17.5 km long, and an area with large, low-relief cratered volcanoes to the NW of the triple junction (centered at 15°30′S, 174°57′W).

To the west of the MTJ-N arm is an area of rifting with inward-dipping faults and no associated neovolcanic zone, which we refer to as the Western Rift assemblage. In the north, the crust is heavily faulted with overlapping zig-zag structures that that trend NNE, NE, and ENE (**Fig. 5b–d**). In the south, the crust is dominated by younger volcanic flows with morphologies characteristic of sheet flows with collapse features and lesser amounts of pillow flows. Volcanic flows become more common to the west towards the subaerial Niuafo'ou volcanic island, located outside the study area. Cross-cutting the dominant NE-fabric of this area are WNW- and NW-trending volcanic ridges and faults (**Fig. 5g–h**). The area has not been previously described or sampled, and therefore the lithology is unknown.

The NELSC assemblage follows a NE-oriented spreading center that consists of four segments and displays a gently sigmoidal shape. The northernmost segment is characterized by a 40-km long axial valley resembling a slow-spreading MOR morphology, while the remaining segments in the south are characterized by axial ridges that are ~15 km in length resembling fast-spreading MOR morphologies. The neovolcanic zone is irregular, between 3.4 and 9.7 km wide. The neovolcanic zone of the northernmost segment consists of elongate hummocky lava flows and mounds. There is a gradual progression southward towards a more flat-topped axial volcanic ridge morphology with point-source volcanic cones. Flat-topped volcanic cones occur near the ends of the NELSC. The southernmost segment is the most magmatically-robust, with axial volcanic ridge highs reaching ~1260 m above the surrounding seafloor, with large volcanic cones on each termination of the ridge (Maka and Tafu). Proximal to the neovolcanic zone is older, faulted crust, followed by distal heavily-sedimented ridges. These ridges are symmetrical,

indicating a volcanic rather than structural origin. Several large volcanic ridges up to 1570 m tall and 24 km long occur distal to the spreading center, notably to the east of the southern NELSC (centered at 15°24′S, 174°08′W) and to the west of the northern NELSC (centered at 14°55′S, 174°15′W). The structures along this spreading segment are dominantly NNE- and NE-trending (**Fig. 5b–c**), with distal N-trending structures associated with volcanic ridges on the SW and NE sides of the spreading center (**Fig. 5a**).

The FRSC overlaps with the MTJ-S and is oriented N-S to accommodate E-W extension between the Niuafo'ou and Tongan microplates (Sleeper & Martinez, 2016). The FRSC consists of at least six overlapping, left-stepping segments that become progressively closer to the arc towards the south, described by Sleeper et al. (2016). The study area includes the three northern segments, which are ~12–27 km long and are characterized by axial valleys containing a neovolcanic zone up to ~15 km wide (**Fig. 3**). Narrow axial volcanic ridges are surrounded by smooth, featureless seafloor that may be sheet flows or volcaniclastic sediment derived from the nearby volcanic arc. The axial valleys are bounded by steep-sided faults, but unlike other spreading segments in the study area, off-axis faulting is not laterally continuous. The valley flanks are dominated by irregular volcanic ridges and numerous small volcanic cones. To the south of the map area, the axial valleys become less pronounced and there is a transition towards axial ridge morphologies. Based on the width of this assemblage (20–30 km) and the inferred spreading rate (26 mm yr^{-1}; Sleeper & Martinez, 2016) at the northern extent of the FRSC, rifting began between 0.8 and 1.1 Ma. In the north there is an area of robust volcanic activity characterized by coalescing volcanic cones and ridges, as well as a large volcanic ridge, 29-km-long and 1350-m-tall, extending towards the MTJ-N (centered at 15°41′S, 174°38′W). The transition between the FRSC and the MTJ-N is difficult to distinguish. The structures along the

FRSC are dominantly N-trending (**Fig. 5a**), with minor NNE- and NNW-trending structures at the northern termination (**Fig. 5b** and **i**).

Finally, an enigmatic area consisting of variably-oriented volcanic ridges that are not clearly associated with a spreading center occur in the NW part of the map area, referred to here as the NW Ridge Assemblage (**Fig. 3**). This area may reflect a distal portion of the NELSC. The ridges are sub-parallel and oriented NNE to NE (**Fig. 5b–c**) and WNW to NNW (**Figs. 5h–i**). The ridges rise to heights of 760 m above the surrounding seafloor. The areas between the ridges is interpreted to be sediment, although backscatter data is lacking in this area and young lava flows may be present. In the north, the ridges are cut by a N-trending rift that extends into the paleo-arc and appears to be heavily sedimented. The curved appearance of some of the ridges may be related to extension along this rift, resembling a large-scale drag fold. The southern contact between this unit and the NW Rift assemblage is poorly defined due to a lack of high-resolution multibeam and backscatter data and may be gradational. The lithology of this assemblage is unknown because it has not yet been sampled.

4.2. Rear-arc volcanism

Volcanism that occurs between the active arc front and the spreading centers is referred to as rear-arc volcanism, which is associated with more siliceous lithologies than the back-arc (e.g., Embley & Rubin, 2018). The Mata volcano assemblage occurs in the NE part of the study and consists of nine elongate en echelon volcanic ridges composed of boninitic pyroclastic material and lava flows, surrounded by lava flows (**Fig. 3**; Resing et al., 2011a; Rubin & Embley, 2012). These volcanoes have been actively erupting over the last 2 Ma, with older occurrences extending into the fore-arc region (Falloon et al., 2008; Rubin & Embley, 2016; Chadwick et al., 2019). The southern volcanoes, West and East Mata, are 1400–1700 m tall and

are elongate along an ENE-trend (**Fig. 5d**). The West Mata volcano is one of only two places in the world where deep-sea submarine eruptions have been witnessed (Resing et al., 2011b). The Mata volcanoes to the north (Taha, Ua, Tolu, Fa, Nima, Ono, Fitu) are smaller (900–1300 m tall) and are variably elongate in ENE- and E-directions.

South of the Mata volcanoes is the Niuatahi assemblage, characterized by the 15-km wide Niuatahi dacite volcano (formerly "Volcano O"), that rises ~1340 m above the surrounding seafloor with a 9-km-wide nested caldera (**Fig. 3**). This volcano is cross-cut by a regional N-trending structure (**Fig. 5a**), with E-W extension indicated by short gaps in the caldera walls in the north and south (Baker et al., 2019). Along this regional structure in the south-central part of the caldera is a 465-m-tall resurgent volcanic cone called Motutahi, which is associated with dacite flows (Park et al., 2015) and active venting (Kim et al., 2009). Niuatahi is surrounded by dacite lava flows that extend ~60 km north and northeastward over an area of ~640 km^2, described by Embley and Rubin (2018). Backscatter signatures indicate at least two ages of flows, with the most recent flows displaying a very high backscatter signal. The chemistry of the flows varies according to location, which Embley and Rubin (2018) use to define three distinct flows, indicating that the eruptions originate from a fissure rather than simply from the Niuatahi volcano. At the map scale here, we group the young flows as a single unit. Lower-than-expected viscosities of these Si-rich lavas are attributed to high magmatic water contents, CO_2 contents, and/or high eruptive temperatures (Embley & Rubin, 2018). These dacite flows surround irregularly-shaped topographic features, which we interpret to be older constructional volcanic features that represent a central fissure system.

311 4.3. Arc volcanism

312 In the study area, the Tofua arc trends ~18–23° in the south and ~5–8° in the north (**Fig.**
313 **3**). This assemblage consists of four units: large arc volcanos (including Volcano L, Volcano K,
314 Niuatoputapu, Tafahi, Curacoa, and other unnamed volcanoes), the Niua volcanic complex,
315 smaller volcanic edifices, and lava flows. The northern portion of the arc has not been sampled
316 extensively; however, four samples were collected during the SO-263 cruise, including one
317 andesite, two basaltic andesites, and one basalt (Haase et al., 2018). This is consistent with
318 sampling along the arc segment adjacent to the FRSC, which is dominantly basaltic andesite
319 (Keller et al., 2008; Sleeper, 2017). The Tofua arc volcanoes are dominantly submarine
320 stratovolcanoes that decrease in size northwards towards the termination of the arc. Many of
321 these volcanoes have large interior caldera structures. Submarine volcanoes K and L, and
322 subaerial volcano Niuatoputapu are all apparently inactive. No historical eruptions have been
323 reported at subaerial Tafahi volcano, but the youthful morphology suggests recent (Holocene)
324 activity (Taylor & Ewart, 1997). A recent eruption at the submarine Curacoa volcano was
325 reported in December 1979 (Global Volcanism Program, 2013). At the northern termination of
326 the arc, the submarine Niua volcanic complex (formerly "Volcano P") has a distinct morphology
327 consisting of numerous overlapping cones and a strongly tectonized appearance. This large
328 complex appears roughly rectangular in plan view, up to 25 km long and 13 km wide, and rises
329 to depths of ~2000 m above the surrounding seafloor. Small (≤100 m tall), dome-like
330 topographic features that are irregularly distributed at the top of the Niua complex are interpreted
331 to be small volcanic edifices. Profuse venting of S-rich magmatic fluids at the Niua North vent
332 site indicate that it is volcanically active (Rubin et al., 2018; Haase et al., 2018). Niua is the only
333 place along the Tofua arc in the map area that has confirmed hydrothermal venting (Niua South
334 vent field; Arculus, 2004). Surrounding the northernmost arc volcanoes are young lava flows that

are identified by high backscatter signatures. We interpret these flows to be genetically related to the Tofua arc volcanoes based on proximity; however, these flows have not been sampled so this relationship is unconfirmed.

4.4. Paleo-arc crust

The paleo-arc assemblage occurs in the northernmost part of the map area and is characterized by a bulging morphology that is heavily tectonized (**Fig. 3**). We include the paleo-fore-arc with this assemblage as the morphology does not allow easy distinction. Few samples from this area have been collected, mainly consisting of adakite and boninite (Falloon et al., 2008; Price et al., 2016). The density of structures in this area is high and includes structures of every orientation (**Fig. 5**). There are some areas adjacent to active back-arc volcanism where the paleo-arc appears to contain volcanic ridges and cones with youthful morphologies that may be capturing magmatism from the back-arc. Backscatter data in these areas is lacking and samples have not been collected. In addition, an area of intensely-faulted terrane to the west of the Mata volcanoes is interpreted to be an area of detached paleo-arc crust. The structural fabric of this block is dominated by WNW-, NW- and NNW-trending fabrics, similar to the paleo-arc crust on the opposite side of the NELSC (**Figs. 5g–i**), and distinct from adjacent assemblages. However, these structural orientations may have been modified during opening of the NELSC, and so the origin remains uncertain. This displaced unit does not show evidence of recent volcanism.

4.5. Sedimentary features

Clastic sediments are ubiquitous throughout the basin (**Fig. 3**), forming a cover sequence that is divided into two units: a rippled volcaniclastic sediment apron that extends from the volcanic arc, and a smooth featureless plain that is likely a combination of pelagic and

volcaniclastic sediment. The contact between these two units is gradational, and the contacts with other units tends to be sharp and can be distinguished by the very low backscatter signature.

4.6. Structural features

A total of 5,892 major fault segments (>100 m throw), 12,071 minor fault segments (< 100 m throw), 7,420 volcanic ridge segments, and 10,624 lineament segments were interpreted and digitized (**Fig. 4**). The distribution of the structural orientations is shown in **Figure 5**. The dominant orientations are N-trending (0–10°; n = 2959) and NE-trending (30–40°; n = 3033), following the orientations of the major spreading centers. Evidence for cross-cutting relationships between the structures is most pronounced in highly tectonized areas, namely, the W Rift zone and the Paleo-Arc crust (**Fig. 5**). Cross-cutting relationships between structures with similar orientations (e.g., N- and NNE-trending) were not observed, instead these features tend to form zig-zag faults. A summary of relative cross-cutting relationships is outlined in **Table 1**, with examples shown in **Fig. 4c, d**. In general, these relationships indicate that the oldest structures are NNW-, NW-, and WNW-trending, intermediate-age structures are NE- and NNE-trending, and the youngest structures are N-, W-, E-, and ENE-trending.

4.7. Escarpments

There is a distinct three-tiered down-dropped basin topography across the NE Lau Basin (**Fig. 2**). The borders of these tiers are defined by large escarpments with throws of up to 1500 m, which are some of the most striking features in the basin (**Figs. 3** and **4a**). A large escarpment in the NE map area ("Escarpment A" in **Fig. 3**) forms the wall of the ~NNW-trending basin that hosts the Mata volcanoes and the Niua arc volcano. This escarpment is ~30 km long in the map area and has a maximum throw of 890 m. The dip of this escarpment is variable across its length, averaging 36° to the NNE. One dredge sample from this escarpment was dated at 2.03±0.11 Ma

380 **Table 1.** Cross-cutting relationships of structures according to orientation (examples in **Fig. 4c, d**)

Structure by orientation	Cross-Cut By	Cross-Cuts	Shear Sense
NNW-trending	N, NNE, NE, E, W		
NW-trending	N, NNE, NE, ENE, E		
WNW-trending	N, NNE, NE, ENE, E		
NE-trending	N, ENE, E, W	WNW, NW, NNW	Unknown (offset minor)
NNE-trending	ENE, E	WNW, NW, NNW	R-lateral
N-trending	W	NE, NNW, WNW, NW, W	R-lateral
W-trending	N, ENE	N, NE, NNW	L-lateral
E-trending		NNE, NE, NNW, WNW, NW	L-lateral
ENE-trending		NNE, NE, WNW, NW, W	L-lateral

381

(K-Ar dating; Falloon et al., 2007), although the timing of formation of this escarpment is difficult to constrain due to its association with recent volcanic flows (**Fig. 3**). Another ~62-km-long escarpment with a maximum throw of 1070 m occurs at the southern termination of the NELSC ("Escarpment B" in **Fig. 3**) trending ~ENE towards the arc. The average dip is 24° to the NW. Connected to this escarpment in the south is a ~N trending escarpment ("Escarpment C" in **Fig. 3**) that becomes NNE-trending with increasing latitude. This escarpment extends ~37 km before it is interrupted by the MTJ-N at 15°19′S. It continues on the opposite side for another ~38 km. This part of the escarpment appears to be interrupted by a detachment fault at 15°07′S (mapped as a core complex in **Fig. 3**), characterized by NNW-trending corrugations, although there is a high degree of uncertainty in the identification of this feature. This escarpment appears to comprise multiple stepping faults in places, but in general it has a maximum throw of 1095 m, dipping ~24° to the E and NE. It is intersected by an NNW-trending escarpment ("Escarpment D" in **Fig. 3**) that forms the western boundary of the MTJ-N. This escarpment has a maximum throw of 1085 m, decreasing in size southwards towards normally-faulted terrain of the MTJ. Using a cutoff throw of 500 m to define this escarpment, it has a length of ~23 km, and dips of 22° to the SE. These dip angles are likely an underestimate of the true dips due to erosional processes over time, indicated by mass wasting features at the base of some of the escarpments.

5. Fault kinematics

Two of the primary forces driving plate kinematics in the NE Lau Basin are: (1) arc-parallel extension associated with SE rollback of the Tonga trench, and (2) strike-slip movement associated with asymmetric slab rollback and wrench tectonics along the STEP boundary (e.g., Govers & Wortel, 2005; Embley et al., 2009). Extensional rift-parallel horst-and-graben fault patterns are common across the map area, including within neovolcanic zones and off-axis

terrains along the main spreading centers (**Fig. 4a**). Extensional structural fabrics in the NE Lau basin are characterized by two main structural trends that record the recent stages of back-arc development. The first trend is parallel to sub-parallel with the NELSC and MTJ-N (NNE- to NE-trending; **Fig. 5b, c**). This trend follows the orientation of the Tofua arc between 15°30′S and 17°35′S, and south of the collision zone with the Capricorn Seamount(s) between 18°32′S and 24°0′S (~18–23°; **Figs. 2** and **3**). The second trend is parallel to sub-parallel with the MTJ-S and FRSC (N-trending; **Fig. 5a**). This trend follows the orientation of the Tofua arc north of 15°30′S, and to the north of the Capricorn Seamount(s) collision between 17°35′S and 18°32′S (~5–8°; **Figs. 2** and **3**). Subordinate structures are orthogonal to these trends but also display normal faulting and extensional features, including the NE- and ENE-trending large volcanic ridges near the southern NELSC and within the Mata volcanic group (**Figs. 4** and **5c,d**).

Despite the abundance of normal faulting and spreading center development, shallow normal earthquakes are restricted to the FRSC in the south of the map area ($n = 8$; **Fig. 5a**), as well as the northern tip of the NELSC ($n = 4$; **Fig. 5 b, c**). It is likely that extension in the basin is simply not producing high-magnitude ($M_w > 5$) earthquakes. This may indicate that crustal accretion is dominated by magmatic extension driven by dike injection rather than tectonic extension driven by brittle faulting (e.g., Buck et al., 2005; Ito & Behn, 2008; Anderson et al., 2017).

Notably, strike-slip and oblique-slip faulting is widespread across the study area, with shear sense indicated by offset features (**Table 1**; **Fig. 4c, d**) and high-magnitude earthquake focal mechanisms (**Fig. 5**). The main N- and NNE-trending structures (along with minor NNW-trending structures) display a right-lateral shear sense (**Fig. 5a, b, i**), accounting for 73% of shallow strike-slip CMT solutions in the area. In contrast, NE-trending structures do not display

strike-slip motion; instead, these structures may be associated with pure low-magnitude normal faulting with no oblique motion. Subordinate NE-, ENE-, E-, W-, NNW-trending structures display a left-lateral shear sense (**Fig. 5d–g**), accounting for 27% of the shallow strike-slip CMT solutions. The left-lateral CMTs occur near the STEP boundary (n = 7), likely caused by slip between the northern microplates and the Pacific Plate, and farther to the south along the W Rift, MTJ-W, and northern FRSC (n = 19). Dip-slip faults also occur along the STEP boundary east of the NELSC, trending NE, E, W, and WNW (n = 12; **Fig. 5c, e–g**).

The abundance and distribution of strike-slip faulting supports the null-hypothesis that wrench-tectonics dominate the NE Lau basin—extending as far south as ~16°S where strike-slip CMT solutions terminate abruptly—driven by the left-lateral motion along the plate boundary along with asymmetrical hinge-rollback. There is no evidence for slip along the inferred southern boundary of the wrench zone (dashed lines in **Fig. 6**), which instead is dominated by a diffuse zone of seismicity. This is consistent with other edge-driven microplate rotation models (e.g., Schouten, 1993).

We relate the distribution and orientation of right-lateral and left-lateral strike-slip faults within the rigid block boundaries to Riedel shear mechanisms typical of wrench zones, revealing two distinct sets of structures (**Fig. 6**). The first set of Riedel shears are dominated by NNE-trending R′-shears, with minor E-trending R-shears and NNW-trending P-shears (Model 1: **Fig. 6a**). The R'-shears are oriented at a high angle (~75°) counter-clockwise to the boundaries of the wrench zone, which trend ~95° following the orientation of the northern plate boundary. The R'-shears follow the main trends along the NELSC and the W Rift zone and are sub-parallel to MTJ-N. Typically, R′-shears may develop with or after R-shears (e.g., Atmaoui et al., 2006), which are oriented ~10–15° counter-clockwise and synthetic to the wrench zone boundaries. In

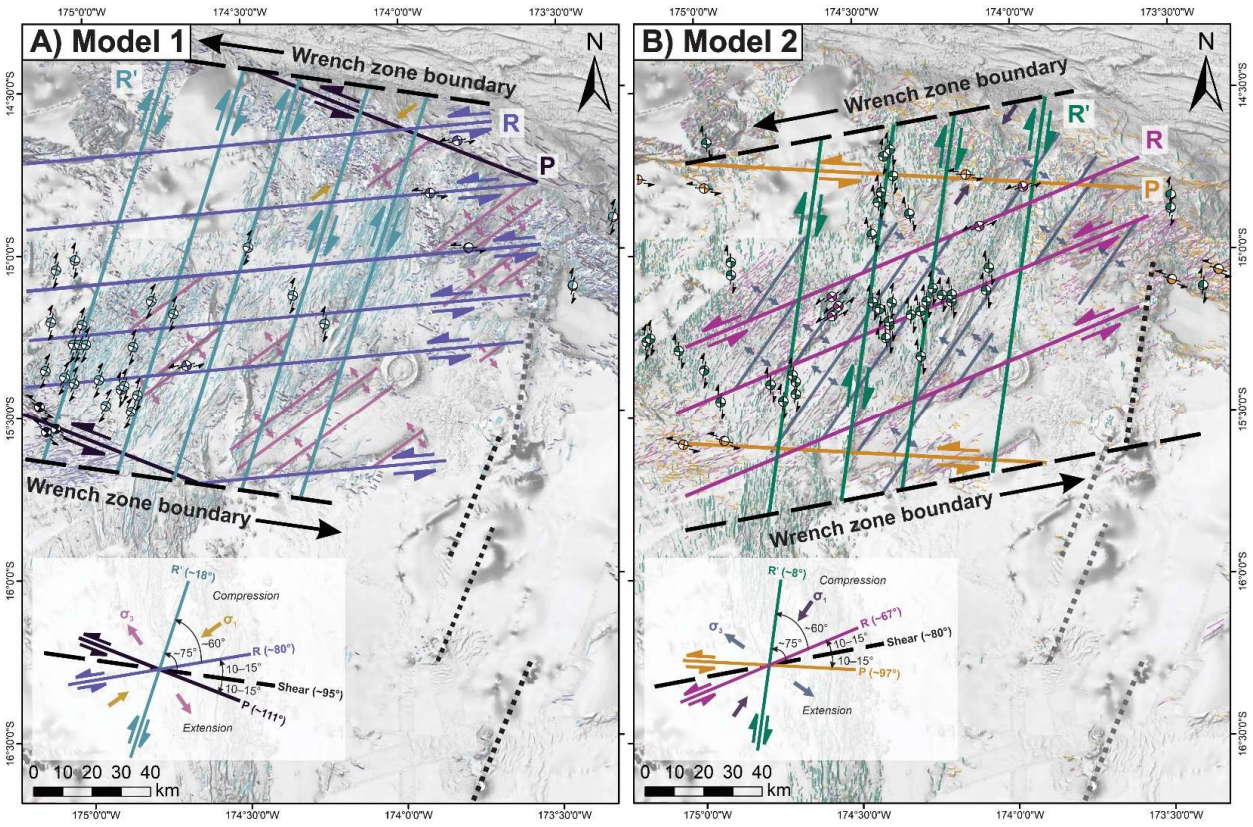

Figure 6. Riedel shear mechanisms associated with strike-slip faulting in a wrench zone overlain on greyscale-shaded bathymetry with associated lineaments, showing two configurations: (a) Model 1, with shear zone boundaries oriented ~98° dominated by NNE-trending R′-shears that are parallel to the southern Tofua Arc segments, with active seismicity mostly restricted to the western map area, and (b) Model 2, with shear zone boundaries rotated counter-clockwise to ~80° dominated by N-trending R′-shears that are parallel to the northern Tofua Arc segment, with active seismicity dominating the central map area. Extension associated with σ_3 is offset by R-shears and is associated with large volcanic ridges across the map area in both configurations. Bathymetric data sources as in **Fig. 2** and CMT focal mechanisms as in **Fig. 5**.

461 the study area, R-shears are not widespread, but closely align with the structural trend of the
462 eastern Mata volcanoes and a well-developed strike-slip fault zone in the northwest map area.
463 The P-shears are more difficult to identify but may be manifest as the WNW-trending fabrics in
464 the southern and northern parts of the map area. Within this configuration, compression
465 associated with σ_1 may produce the bulging morphology of the paleo-arc crust, and extension
466 associated with σ_3 is associated with the large ENE-trending volcanic ridges at the southern end
467 of the NELSC, as well as West and East Mata. The orientation of these structures is oblique to
468 the direction of hinge-rollback, suggesting that normal back-arc spreading processes cannot
469 account for all the extension in this area. These extensional features are offset by the R-shears,
470 creating an extensional duplex (**Fig. 5**). North of the FRSC, there appears to be a cluster of NNE-
471 trending seismicity associated with left-lateral fault motion, contrasting the right-lateral motion
472 of faults along other NNE-trending CMTs in the region (**Fig. 5b**). Sleeper (2017) suggests that
473 these strike-slip events are due to a zone of transferred lithosphere, although the regional
474 kinematic control on this reversal is unclear. We therefore interpret the southernmost diffuse
475 boundary of the wrench zone to occur near Escarpment B (**Figs. 3** and **6b**).
476 The second set of Riedel shears are similar but rotated ~8–12° counter-clockwise relative
477 to the first set of shears (Model 2: **Fig. 6b**). These shears are dominated by N-trending R′-shears,
478 with minor ENE-trending R-shears and W-trending P-shears. The R′-shears follow the
479 orientation of MTJ-S and FRSC, the N-trending fissure system extending north of the Niuatahi
480 volcano, and other N-trending features in the area. The R-shears follow the trend of the southern
481 and eastern Mata volcanoes and the large volcanic ridge to the west of Niuatahi, apparently re-
482 activating previous extensional fabric. The wrench zone boundaries trend ~80°, following the
483 previous orientation of R-shears in Model 1 (**Fig. 6a**), and sub-parallel to the orientation of

Escarpment B in the south (dashed lines in **Fig. 6**). Notably, the orientation of the wrench zone parallels the major Fonualei Discontinuity that offsets the arc to the south of the study area (**Fig. 2**). P-shears are also poorly defined for this configuration, but match strike-slip faulting near the northern and southern boundaries of the wrench zone. In this configuration, extension along σ_3 is associated with NE-trending volcanic ridges across the map area, such as the western Mata volcanoes, which are offset by R-shears. This extensional fabric is also parallel to the MTJ-N, the West Rift zone, and the northern and southern terminations of the NELSC and may be enhancing spreading associated with hinge-rollback.

The differing distribution of fault populations from a typical Riedel shear zone (dominated by R-shears) is likely because R′-shears occur at an angle similar to that of faults produced by earlier back-arc extension. It is easier to reactivate these pre-existing faults as opposed to creating new ones as the stress required for frictional sliding along pre-existing faults is much less than the fracture strength (e.g., Byerlee, 1978). Similarly, as the stress-field rotated, pre-existing extensional faults were re-activated as R-shears. This effect has been observed in other back-arc basins (e.g., Manus Basin: Martinez & Taylor, 1996; Morley et al., 2004; Maestro-González et al., 2008). Faults that have undergone strike-slip reactivation tend to have zig-zag geometries with little throw. These morphologies are common throughout the map area but are particularly well-defined in the western part of the map area in the West Rift zone and the MTJ-W arm. Therefore, the observed strike-slip kinematics in the study area support a rigid block model of lithospheric-scale Riedel shearing, where shearing reactivates pre-existing extensional faults. This indicates that structures in wrench zones may be predisposed to align themselves to the pre-existing fabrics in back-arc settings.

6. Discussion

6.1. Tectonic evolution of the NE Lau Basin

The occurrence of two different Riedel shear geometries in the NE Lau Basin (Models 1 and 2; **Fig. 6**) indicates that the stress field has rotated over time. Structures associated with both geometries are distributed across the map area; however, active seismicity associated with Model 1 (dominated by NNE-trending R′-shears) occurs mainly in the western portion of the map area, while seismicity associated with Model 2 (dominated by N-trending R′-shears) occurs in the central portion of the map area closest to the active arc. Cross-cutting relationships indicate that Model 2 structures generally are the youngest (**Table 1**). We propose that this structural configuration is driven by a recent, large-scale tectonic re-organization of the NE Lau Basin, outlined in **Figure 7**. Prior to ca. 1 Ma, the Tofua Arc formed a relatively continuous chain of volcanoes, oriented ~18–23°. The hinge point for large-scale fore-arc rotation was near the Louisville seamount collision at ~175°W and ~24°S (Wallace et al., 2005). Back-arc extension associated with hinge rollback formed the NELSC and MTJ-N parallel to the arc (**Fig. 7a**). While several authors suggest that the FRSC is the most recently formed spreading center in the Lau Basin (e.g., Zellmer & Taylor, 2001), the fact that some of the FRSC segments are NNE-trending (FRSC 4 and 5 in Sleeper et al., 2016) indicates that the proto-FRSC may have started to develop during this time. Wrench tectonics in the northern part of the Lau Basin was driven by transform motion along the STEP boundary that resulted in abundant strike-slip faulting, which was dominated by NNE-trending R′-shears oriented along the extensional fabric of the basin (**Fig. 6a**).

Subsequently, the Capricorn Seamount(s) collided with the Tonga trench (**Fig. 7b**). This induced slip in the upper plate at the Fonualei Discontinuity (FD), which segmented the rotating fore-arc block. As the northern block became bound by strike-slip faults, eastward slip along

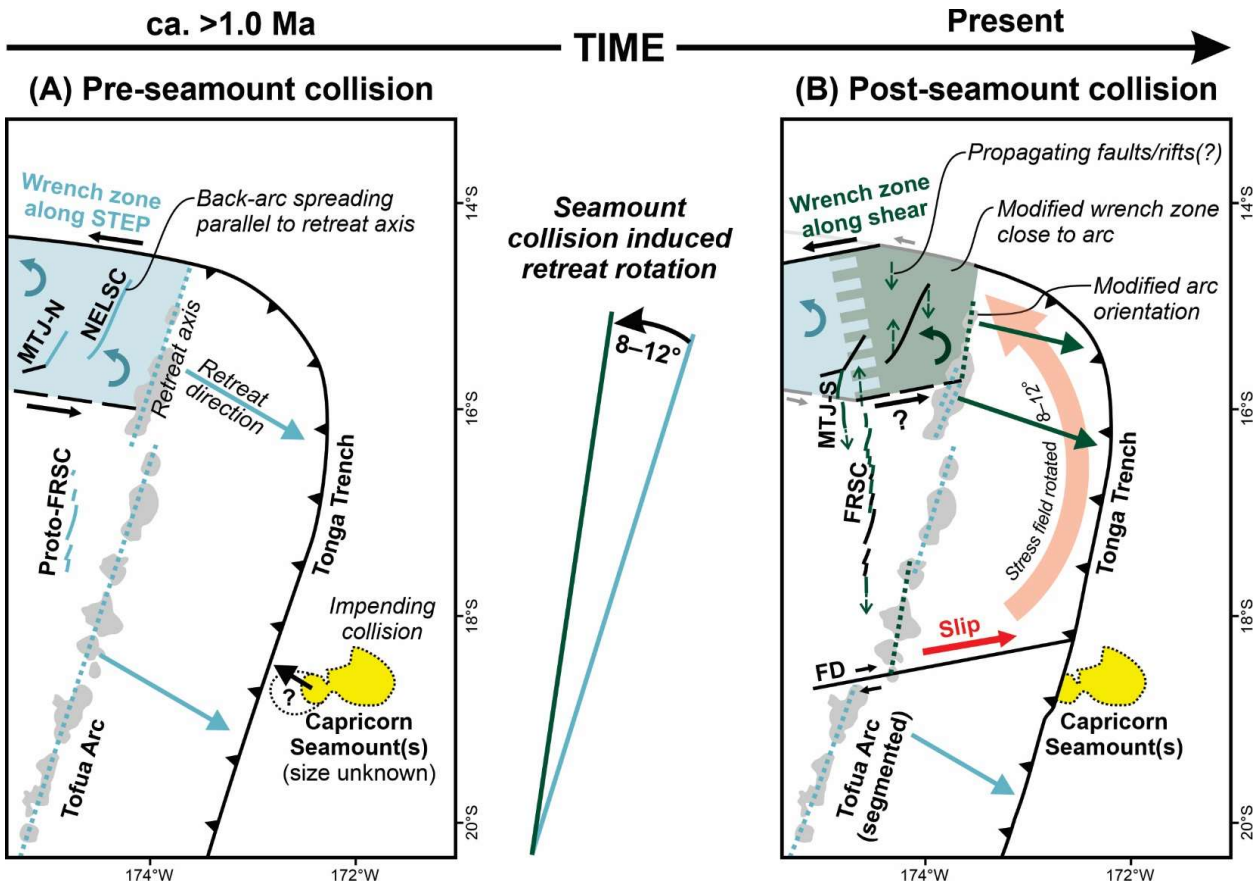

Figure 7. Model of the recent tectonic evolution of the NE Lau Basin: (a) prior to collision with the Capricorn Seamount(s), the trench-arc system was trending NNE, associated with the development of the NELSC and MTJ-N. Wrench tectonics in the north are driven by transform motion along the STEP and asymmetric slab rollback (i.e., Model 1 in **Fig. 6**); and (b) collision with the Capricorn Seamount(s) induced slipping along the Fonualei Discontinuity (FD) adjacent to the collision zone, and caused the northern block to become bound by strike-slip faults. Eastward movement along the southern FD boundary combined with westward movement caused by friction along the northern boundary produced an 8–12° counter-clockwise rotation of stress field. This caused segments of the arc volcanoes to re-orient to a more northerly direction, and modified the angle of retreat, triggering the propagation of new spreading centers (FRSC, MTJ-S) as well as smaller propagating faults/rifts in the northern basin. The modified stress field triggered new Riedel shear mechanisms in the area closest to the arc (i.e., Model 2 in **Fig. 6**) associated with non-rigid plate kinematics. The new wrench zone boundaries align with the trend of the FD and pre-existing R-shears produced during earlier Riedel shearing in the wrench zone. Further west of the arc, the original wrench structures (Model 1) remain seismically active, with a gradual transition to the modified wrench configuration. Note that the pre-collision size of the Capricorn Seamount(s) is unknown, and the absolute timing of collision and rift development is poorly constrained. Present day GPS plate vectors from Phillips (2003).

548 the southern FD boundary may have been accompanied by westward-directed stress along the
549 northern boundary caused by friction. These combined effects promoted a counter-clockwise
550 rotation of the stress field of the northern block by 8–12°. This re-oriented some of the Tofua Arc
551 segments to a more northerly direction (~5–8°), and the reorientation of the extensional axis
552 caused spreading along the MTJ-S and FRSC (**Fig. 7b**). Additional evidence for the development
553 of the FRSC under a changing tectonic regime is provided by Sleeper and Martinez (2016), who
554 link the dynamic history of rotation and opening of the northern Lau Basin with complex
555 asymmetrical structural and volcanic features on the flanks of FRSC. Within the wrench zone,
556 internal plate deformation triggered the formation of Model 2 Riedel shear geometries under this
557 new stress field, primarily affecting the area closest to the arc. In this scenario, the re-activation
558 of faults was favored over the formation of new faults. This work supports the idea that non-rigid
559 plate kinematics are important in the development of the northern Lau Basin, as described by
560 Sleeper and Martinez (2016).

561 A remaining question is whether the collision of an apparently small topographic feature
562 like the Capricorn Seamount(s) can induce such dramatic changes in the stress of the overriding
563 plate. The size of the already-subducted portion of this seamount is unknown, but remaining
564 portion of the seamount rises to ~3200 m from the surrounding seafloor, and the apparent length
565 of the affected trench (indicated by topographic irregularities) is ~60 km (**Fig. 2**, inset). This is
566 comparable to the seamounts that comprise the LSC in the south, which rise to ~3500 m from the
567 surrounding seafloor with trench-parallel widths of ~40–70 km (Ruellan et al., 2003). It is also
568 similar to the size of the d'Entrecasteaux Ridge (DER) that is colliding with the central Vanuatu
569 Arc, which is comprised of two parallel ridges that rise 2–3 km above the surrounding seafloor,
570 with widths of 30–40 km, affecting a total length along the trench of ~115 km (e.g., Collot et al.,

1992; Baillard et al., 2018). The effects of the LSC and DER collisions are well-documented, including the effects of plate coupling, locking and unlocking of subduction, arc segmentation, crustal thickening and shortening in the segments adjacent to the collision, reduced back-arc extension, and far-field stresses and associated development of structures (e.g., Charvis & Pelletier, 1989; Meffre & Crawford, 2001; Ruellan et al., 2003; Anderson et al., 2016). In these cases, collision is associated with a strong indentation of the trench and induces rotation of tectonic blocks to the north and/or south of the collision zone (e.g., Wallace et al., 2005; 2009). In contrast, indentation of the trench at the Capricorn collision zone is less pronounced; rather, the predominance of surficial fracturing may result from the ultra-fast subduction rates and/or the size or buoyancy of the subducting seamount(s). This work highlights the importance of terrane collisions in the evolution of subduction zones, which can exert a first-order control on upper plate stresses and associated structures in the back-arc over large areas, providing conduits for magmas to reach the seafloor.

6.2. Structural controls on magmatic-hydrothermal activity

One of the most striking features of the NE Lau Basin is the decentralized nature of volcanism on the seafloor, manifest by large off-axis volcanic ridges, hydrothermally-active rear-arc volcanoes, and widespread lava flows (**Fig. 3**). Previous authors propose that the Mata rear-arc volcanoes are controlled by small crustal tears linked to strike-slip faulting along the STEP boundary (Govers & Wortel, 2005; Embley et al., 2009), but these authors do not provide an explanation for the variable orientations of the Mata volcanoes, along with other enigmatic features such as the siting of the Niuatahi volcano. The structural framework outlined here provides insight into the occurrence of many of these seafloor features. Notably, large volcanic ridges reflect areas of enhanced magmatism in the map area, and are aligned along several

orientations: (1) NNE-trending ridges, including southern Mata volcanoes and the large volcanic ridges at the southern end of the NELSC; (2) E-trending ridges forming the western Mata volcanoes; (3) N-trending ridges, including the large ridge to the north of the FRSC and the subtle ridge extending northward from Niuatahi. In this configuration, NNE- and E-trending features formed early associated with σ_3 extensional structures in the Model 1 configuration (**Fig. 6a**). These structures were then reactivated as R-shears (Model 2 configuration), along with the formation of the N-trending features during back-arc extension and subsequent re-activation as R′-shears during strike-slip faulting (**Fig. 6b**). In the most recent configuration, extension also occurs along NE-trending structures associated with the new σ_3 orientation. This promotes enhanced magmatism along the southern NELSC and the MTJ-N, as well as rifting along the W Rift zone. We also note that the large Niuatahi rear-arc volcano occurs at the intersection of N-trending and NNE-trending structures. These structures, which have not been previously described, but are underlain by linear magnetic anomalies (Austin, 2012), indicating that magma is exploiting these structural pathways. Dacitic sheet flows at surface extend ~60 km northward from Niuatahi, apparently following a N-trending fissure rather than erupting from the volcano itself (Embley & Rubin, 2018). Within the Niuatahi caldera, hydrothermal vents are also aligned along this N-trending regional structure (**Fig. 3**; Haase et al., 2018). Across the map area, hydrothermal vents are closely associated with these regions of enhanced magmatism. Continual re-activation of faults may ensure that these pathways remain permeable despite precipitation of secondary hydrothermal minerals. This complex structural configuration, combined with unusually high upper mantle temperatures and ultrafast subduction rates (e.g., Regelous, 2008), provides the basis for diverse lithologies and eruption styles in the basin, along with a range of

616 style and composition of hydrothermal venting (e.g., Embley & Rubin, 2018; Chadwick et al.,
617 2019).

618 6.2. Links to microplate emergence

619 Much of our understanding of the emergence of microplates comes from studies in mid-
620 ocean ridge (MOR) settings where plate reorganizations are linked to the propagation of new
621 rifts, forming the boundaries of new microplates (e.g., Wiedicke & Habler, 1993). In contrast,
622 few studies have investigated how these processes operate in back-arc settings where rift
623 propagation is due to subduction-related processes, and the thermal structure of the crust is
624 affected by arc magmatism. Processes such as asymmetric spreading, arc-ward ridge migration,
625 basin-ward arc migration, and the general short-lived nature of spreading centers are common in
626 back-arc basins and less common in MOR settings (e.g., Parson et al., 1990; Martinez and
627 Taylor, 2003). In the NE Lau Basin, we demonstrate the structural effects of a plate
628 reconfiguration associated with the collision of the Capricorn Seamount(s), which has changed
629 the orientation of the extensional axis along a new northward trend. As the extensional axis
630 changes, there is a tendency for rifts to propagate outwards from the tips along the new
631 extensional axis (e.g., CLSC: Parson et al., 1990). This process may be quicker when
632 propagation occurs in thinner crust and where back-arc retreat is the greatest (Parson et al.,
633 1990). The plate reconfiguration associated with the Capricorn Seamount(s) collision may have
634 induced the propagation of new rifts, such as FRSC segments. Simultaneous northward
635 propagation of the FRSC and southward propagation of the MTJ-S produce a zone where the
636 spreading centers overlap, and we observe oblique and curved structural patterns that are
637 characteristic of overlapping spreading centers (North Fiji Basin: Ruellan et al., 1993). Within
638 the map area, major N-trending structures also appear to be extending northward and southward

639 from both tips of the NELSC, and N-trending rifting is occurring along the paleo-arc crust in the
640 northern part of the map area (**Fig. 7b**). These structures may reflect the early stages of rift
641 propagation, but higher-resolution magnetic data is needed to investigate the nature of these
642 features.

643 The re-orientation of the stress field has mainly affected the area closest to the arc,
644 preserving the original wrench zone configuration in the west where it remains seismically active
645 (**Fig. 6**). This suggests that the eastern portion of the NE Lau Basin may be in the nascent stages
646 of nanoplate emergence, proposed by Conder and Wiens (2011) as the separate "Niuatoputapu"
647 plate. This is supported by a drastic change in the structural fabric of the basin from west to east
648 across Escarpment C (**Figs. 3–5**). The fabric to the west of this escarpment is dominated by zig-
649 zagging normal-faulted terrane of the West Rift assemblage, and to the east of this escarpment
650 are the N- and NNE-trending volcanic ridges of the NW Ridge and NELSC assemblages. Like
651 other back-arc micro- and nanoplates, the precise boundaries of Niuatoputapu are difficult to
652 define, and may remain only partially separated, as is the case in the southern diffuse boundary
653 of the Niuafo'ou microplate (**Fig. 2**; Sleeper & Martinez, 2016). In back-arc basins, we expect
654 frequent plate reconfigurations associated with seamount collisions. Depending on the stress
655 response in the upper plate, this may provide a mechanism for the generation of mosaics of
656 microplates in back-arc settings (e.g., Mann et al., 1995). However, in the NE Lau Basin this
657 effect may be short-lived and episodic, limited to the duration of the collisional event and
658 associated block movements. It is yet unknown whether a microplate can develop over these
659 short timescales, or if it requires longer-lived processes to fully emerge. Due to the transient
660 nature of this process, it is likely overlooked in the geologic record as kinematic reconstructions
661 are based on magnetic data that may not provide high-enough temporal resolution (e.g., Sleeper

& Martinez, 2016). However, this may be an important process in the development of structures that play a continued role in the magmatic, and hydrothermal evolution of the back-arc.

7. Conclusions

Compared to mid-ocean ridges, back-arc spreading centers are ephemeral features that evolve dynamically in response to oblique convergence, subduction-zone collisions, and microplate interactions. The NE Lau Basin is characterized by extreme tectonic complexity, associated with fast convergence rates, high upper mantle temperatures, and thin oceanic crust (Bevis, et al., 1995; Conder & Wiens, 2006, Embley, 2018), producing diverse lithologies and eruption styles in the rear-arc and back-arc regions (e.g., Embley & Rubin, 2018). This complexity is manifest as seafloor fabrics with variably-oriented structures. The observed structural patterns reflect the interplay between extension associated with slab-rollback and strike-slip faulting associated with wrench tectonics along the northern STEP boundary. Two distinct sets of structures associated with Riedel shear mechanisms are described for the first time, indicating a recent counter-clockwise rotation of the stress field that primarily affects the region closest to the arc. The structural configurations highlight the importance of re-activation of earlier-formed structures during rotation of the stress-field. The structures that formed and were re-activated in this wrench zone account for the orientations of many of the seafloor features observed, such as the Mata volcanoes and large off-axis volcanic ridges, providing additional insight into the tectonic controls on enhanced magmatism along the southern NELSC and the Niuatahi volcano, as well as the distribution of hydrothermal vent sites in the region. The rotation of the stress field provides evidence for a large-scale tectonic re-organization of the NE Lau Basin, which we interpret to be caused by slipping along the Fonualei Discontinuity induced by the collision of the Capricorn Seamount(s), coupled with westward transform motion along

the northern STEP boundary. This plate reconfiguration likely triggered the propagation of FRSC segments, and minor propagation of N-trending faults and rifts in the northernmost back-arc. As seamount collisions are common features of subduction zones, this mechanism for inducing propagating rifts may be important in the formation of new microplates in back-arc settings.

Acknowledgments

Cruise data related to this manuscript is available online: TN234 from Resing et al. (2009); KM1024 from Rubin et al. (2010); KM1129 from Martinez et al. (2013); FK171110 from Rubin et al. (2018); and SO263 from Haase et al. (2018). Supporting information is provided in the electronic appendix associated with this publication. We appreciate the efforts of the SO-263 Shipboard Scientific Party, ROV QUEST team, and Captain O. Meyer and his crew on R/V Sonne for their contributions and support. We also thank the FK171110 Shipboard Scientific Party and crew of the R/V Falkor, and the support of the Schmidt Ocean Institute. We gratefully acknowledge S. Panasiuk for her assistance with bathymetric post-processing using the TTS-shader, and L. Calhoun for valuable feedback on the structural interpretations. The funding for the project 03G0263 by the German Bundesministerium für Bildung und Forschung is gratefully acknowledged. MOA acknowledges funding from NSERC-DG and the Connaught New Researcher program (UofT). This is contribution MERC-ME-2020-003 to the modern-ancient crust project of the Canadian Metal Earth program.

References

Anderson, M. O., Hannington, M. D., Haase, K., Schwarz-Schampera, U., Augustin, N., McConachy, T. F., & Allen, K. (2016). Tectonic focusing of voluminous basaltic eruptions in magma-deficient backarc rifts. *Earth and Planetary Science Letters*, *440*, 43–55. https://doi.org/10.1016/j.epsl.2016.02.002

Anderson, M. O., Chadwick, W. W. Jr., Hannington, M. D., Merle, S. G., Resing, J. A., Baker, E. T., Butterfield, D. A, Walker, S. L, & Augustin, N. (2017). Geological interpretation of volcanism and segmentation of the Mariana back-arc spreading center between 12.7°N and 18.3°N. *Geochemistry, Geophysics, Geosystems*, *18*, 2240–2274. https://doi.org/10.1002/2017GC006813

714 Aruculus, R., & Shipboard Scientific Party (2004). Voyage Summary SS06/2004: Submarine
715 volcanic and hydrothermal activity in the New Hebrides arc-backarc system. *CSIRO Marine*
716 *Research*. Hobart, Australia: CSIRO. Retrieved from
717 http://www.cmar.csiro.au/datacentre/process/data_files/cruise_docs/ss2004_v06_summary.p
718 df

719 Atmaoui, N., Kukowski, N., Stöckhert, B., & König, D. (2006). Initiation and development of
720 pull-apart basins with Riedel shear mechanism: insights from scaled clay experiments.
721 *International Journal of Earth Sicences*, *95*, 225–238. https://doi.org/10.1007/s00531-005-
722 0030-1

723 Augustin, N., van der Zwan, F. M., Devey, C. W., Ligi, M., Kwasnitschka, T., Feldens, P.,
724 Bantan, R. A., & Basaham, A. S. (2016). Geomorphology of the central Red Sea rift:
725 Determining spreading processes. *Geomorphology*, *274*, 162–179.
726 https://doi.org/10.1016/j.geomorph.2016.08.028

727 Austin, R. A. (2012). Early seafloor spreading and variations in crustal accretion in the Lau basin
728 (Doctoral dissertation). Retrieved from ScholarSpace.
729 (https://scholarspace.manoa.hawaii.edu/handle/10125/100916). Honolulu, HI: University of
730 Hawai'i at Manoa.

731 Baillard, C., Crawford, W. C., Ballu, V., Pelletier, B., Garaebiti, E. (2018). Tracking subducted
732 ridges through intermediate-depth seismicity in the Vanuatu subduction zone. *Geology*, *46*,
733 767–770. https://doi.org/10.1130/G45010.1

734 Baker, E. T., Walker, S. L., Massoth, G. J., & Resing, J. A. (2019). The NE Lau Basin:
735 Widespread and abundant hydrothermal venting in the back-arc region behind a superfast

subduction zone. *Frontiers in Marine Science*, *6*, 382. https://doi.org/10.3389/fmars.2019.00382

Baxter, A. T., Hannington, M. D., Stewart, M. S., Emberley, J. M., Breker, K., Krätschell, A., Petersen, S., Brandl, P. A., Klischies, M., Mensing, R., & Anderson, M. O. (2020). Shallow seismicity and the classification of structures in the Lau back-arc basin. Manuscript submitted for publication.

Beaulieu, S. E., & Szafranski, K. (2019). InterRidge Global Database of Active Submarine Hydrothermal Vent Fields, Version 3.4. Retrieved from http://vents-data.interridge.org.

Bevis, M., Taylor, F. W., Schutz, B. E., Recy, J., Isacks, B. L., Helu, S., Singh, R., Kendrick, E., Stowell, J., Taylor, B., & Calmantli, S. (1995). Geodetic observations of very rapid convergence and back-arc extension at the Tonga arc. *Nature*, *374*, 249–251. https://doi.org/10.1038/374249a0

Bird, P. (2003). An updated digital model of plate boundaries. *Geochemistry, Geophysics, Geosystems*, *4*, 1027. https://doi.org/10.1029/2001GC000252

Bonnardot, M. -A., Régnier, M., Ruellan, E., Christova, C., & Tric, E. (2007). Seismicity and state of stress within the overriding plate of the Tonga-Kermadec subduction zone. *Tectonics*, *26*, TC5017. https://doi.org/10.1029/2006TC002044

Brown, L. (2014, April 25). *Texture Shading: A new technique for depicting terrain relief*. Paper presented at the 15^{h} ICA Mountain Cartography Workshop, Banff, Canada. Presentation retrieved from https://app.box.com/v/textureshading

Buck, W. R., Lavier, L. L., & Poliakov, A. N. B. (2005). Modes of faulting at mid-ocean ridges. *Nature*, *434*, 719–723. https://doi.org/10.1038/nature03358

Byerlee, J. D. (1978). Friction of rocks. *Pure and Applied Geophysics*, *116*, 615–626. https://doi.org/10.1007/BF00876528

Tontini, F. C., Bassett, D., de Ronde, C. E. J., Timm, C., & Wysoczanski, R. (2019). Early evolution of a young back-arc basin in the Havre Trough. *Nature Geoscience*, *12*, 856–862. https://doi.org/10.1038/s41561-019-0439-y

Chadwick, W. W. Jr., Rubin, K. H., Merle, S. G., Bobbitt, A. M., Kwasnitschka, T., & Embley, R. W. (2019). Recent eruptions between 2012–2018 discovered at West Mata submarine volcano (NE Lau Basin, SW Pacific) and characterized by new ship, AUV, and ROV data. *Frontiers in Marine Science*, *6*, 495. https://doi.org/10.3389/fmars.2019.00495

Charvis, P., & Pelletier, B. (1989). The northern New Hebrides back-arc troughs: history and relation with the North Fiji Basin. *Tectonophysics*, *170*, 259–277. https://doi.org/10.1016/0040-1951(89)90275-8

Chase, C. G. (1978). Extension behind island arcs and motions relative to hot spots. *Journal of Geophysical Research: Solid Earth*, *83*(B11), 5385–5387. https://doi.org/10.1029/JB083iB11p05385

Conder, J. A., & Wiens, D. A. (2011). Shallow seismicity and tectonics of the central and northern Lau Basin. *Earth and Planetary Science Letters*, *304*, 538–546. https://doi.org/10.1016/j.epsl.2011.02.032

Collot, J. Y., Lallemand, S., Pelletier, B., Eissen, J. -P., Glaçon, G., Fisher, M. A., Greene, H. G., Boulin, J., Daniel, J., & Monzier, M. (1992). Geology of the d'Entrecasteaux-New Hebrides Arc collision zone: results from a deep submersible survey. *Tectonophysics*, *212*, 213–241. https://doi.org/10.1016/0040-1951(92)90292-E

780 Dziewonski, A. M., Chou, T. -A., & Woodhouse, J. H. (1981). Determination of earthquake
781 source parameters from waveform data for studies of global and regional seismicity. *Journal*
782 *of Geophysical Research: Solid Earth*, *86*(B4), 2825–2852.
783 https://doi.org/10.1029/JB086iB04p02825

784 Ekström, G., Nettles, M., & Dziewoński, A. M. (2012). The global CMT project 2004–2010:
785 Centroid-moment tensors for 13,017 earthquakes. *Physics of the Earth and Planetary*
786 *Interiors*, *200–201*, 1–9. https://doi.org/10.1016/j.pepi.2012.04.002

787 Embley, R. W., Merle, S. G., Lupton, J. E., Resing, J., Baker, E. T., Lilley, M. D., Arculus, R. J.,
788 & Crowhurst, P. V. (2009). *Extensive and Diverse Sumbarine Volcanism and Hydrothermal*
789 *Activity in the NE Lau Basin*. Paper presented at the American Geophysical Union Fall
790 Meeting 2009, San Francisco, CA. Abstract retrieved from
791 https://ui.adsabs.harvard.edu/abs/2009AGUFM.V51D1719E/abstract

792 Embley, R. W., & Rubin, K. H. (2018). Extensive young silicic volcanism produces large deep
793 submarine lava flows in the NE Lau Basin. *Bulletin of Volcanology*, *80*, 36.
794 https://doi.org/10.1007/s00445-018-1211-7

795 Escrig, S., Bézos, A., Langmuir, C. H., Michael, P. J., & Arculus, R. (2012). Characterizing the
796 effect of mantle source, subduction input and melting in the Fonualei Spreading Center, Lau
797 Basin: Constraints on the origin of the boninitic signature of the back-arc lavas.
798 *Geochemistry, Geophysics, Geosystems*, *13*, Q10008.
799 https://doi.org/10.1029/2012GC004130.

800 Falloon, T. J., Malahoff, A., Zonenshaina, L. P., & Bogdanova, Y. (1992). Petrology and
801 geochemistry of back-arc basin basalts from Lau Basin spreading ridges at 15°, 18° and
802 19°S. *Mineralogy and Petrology*, *47*, 1–35. https://doi.org/10.1007/BF01165295

803 Falloon, T. J., Danyushevsky, L. V., Crawford, T. J., Maas, R., Woodhead, J. D., Eggins, S. M.,
804 Bloomer, S. H., Wright, D. J., Zlobin, S. K., & Stacey, A. R. (2007). Multiple mantle plume
805 components involved in the petrogenesis of subduction-related lavas from the northern
806 termination of the Tonga arc and northern Lau Basin: Evidence from the geochemistry of arc
807 and backarc submarine volcanics. *Geochemistry, Geophysics, Geosystems*, *8*, Q09003.
808 https://doi.org/10.1029/2007GC001619

809 GEBCO Compilation Group (2019). GEBCO 2019 Grid [dataset]. doi:10.5285/836f016a-33be-
810 6ddc-e053-6c86abc0788e

811 Global Volcanism Program (2013). Volcanoes of the World, v. 4.8.6. Venzke, E (ed.).
812 Smithsonian Institution. Retrieved from https://doi.org/10.5479/si.GVP.VOTW4-2013

813 Govers, R., & Wortel, M. (2005). Lithosphere tearing at step faults: Response to edges of
814 subduction zones. *Earth and Planetary Science Letters*, *236*, 505–523.
815 https://doi.org/10.1016/j.epsl.2005.03.022

816 Haase, K., & Shipboard Scientific Party (2018). SO-263 cruise report Tonga Rift.
817 *Wochenberichte und short cruise reports*. Hamburg, Germany: Universität Hamburg.
818 Retrieved from https://www.ldf.uni-hamburg.de/sonne/wochenberichte/wochenberichte-
819 sonne/so263-265/so263-scr.pdf

Hall, R. (2002). Cenozoic geological and plate tectonic evolution of SE Asia and the SE Pacific: computer-based reconstructions, model and animations. Journal of Asian Earth Science, 20, 353–431. https://doi.org/10.1016/S1367-9120(01)00069-4

Hall, R., & Spakman, W. (2002). Subducted slabs beneath the eastern Indonesia-Tonga region: Insights from tomography. *Earth and Planetary Science Letters*, *201*, 321–336. https://doi.org/10.1016/S0012-821X(02)00705-7

Hawkins, J. W. (1995). The geology of the Lau Basin. In B. Taylor (Ed.), *Backarc Basins: Tectonics and Magmatism* (pp. 63–138). New York, NY: Plenum Press.

Heuret, A., & Lallemand, S. (2005). Plate motions, slab dynamics and back-arc deformation. *Physics of the Earth and Planetary Interiors*, *149*, 31–51. https://doi.org/10.1016/j.pepi.2004.08.022

Hey, R. N., Johnson, P., Martinez, F., Korenaga, J., Somers, M., Hugget, Q., LeBas, T., Rusby, R., & Naar, D. (1995). Plate boundary reorganization at a large-offset, rapidly propagating rift. *Nature*, *378*, 167–170. https://doi.org/10.1038/378167a0

Ito, G., & Behn, M. D. (2008). Magmatic and tectonic extension at mid-ocean ridges: 2. Origin of axial morphology. *Geochemistry, Geophysics, Geosystems*, *9*, Q09O12. https://doi.org/10.1029/2008GC001970

Karig, D. E. (1970). Ridges and basins of the Tonga-Kermadec island arc system. *Journal of Geophysical Research*, *75*, 239–254. https://doi.org/10.1029/JB075i002p00239

Keller, N. S., Arculus, R. J., Hermann, J., & Richards, S. (2008). Submarine back-arc lava with arc signature: Fonualei Spreading Center, northeast Lau Basin, Tonga. *Journal of Geophysical Research: Solid Earth*, *113*, B08S07. https://doi.org/10.1029/2007JB005451

842 Kim, J., Son, J. -W., Kim, K. -H., Shim, W. J., Kim, C. H., Lee, K. -Y. (2009). Venting sites
843 along the Fonualei and Northeast Lau Spreading Centers and evidence of hydrothermal
844 activity at an off-axis caldera in the northeastern Lau Basin. *Geochemical Journal*, *43*, 1–13.
845 https://doi.org/10.2343/geochemj.0.0164

846 Klischies, M., Petersen, S., & Devey, C. W. (2019). Geological mapping of the Menez Gwen
847 segment at 37°50′N on the Mid-Atlantic Ridge: Implications for accretion mechanisms and
848 associated hydrothermal activity at slow-spreading mid ocean ridges. *Marine Geology*, *412*,
849 107–122. https://doi.org/10.1016/j.margeo.2019.03.012

850 Langmuir, C. H., Bézos, A., Escrig, S., & Parman, S. W. (2006). Chemical Systematics and
851 Hydrous Melting of the Mantle in Back-Arc Basins. In D. M. Christie, C. R. Fisher, S. -M.
852 Lee, & Givens, S. (Eds.). *Back-Arc Spreading Systems: Geological, Biological, Chemical,*
853 *and Physical Interactions* (Vol. 166, pp. 87–146. Washington, DC:American Geophysical
854 Union, Geophysical Monograph Series. https://doi.org/10.1029/166GM07

855 Lupton, J., Rubin, K. H., Arculus, R., Lilley, M., Butterfield, D., Resing, J., et al. (2015). Helium
856 isotope, He, and Ba-Nb-Ti signatures in the northern Lau Basin: Distinguishing arc, back-arc,
857 and hotspot affinities: Helium and Carbon in Northern Lau Basin. *Geochemistry, Geophysics,*
858 *Geosystems*, *16*, 1133–1155. https://doi.org/10.1002/2014GC005625

859 Maestro-González, A., Bárcenas, P., Vázquez, J. T., & Díaz-del-Río, V. (2008). The role of
860 basement inheritance faults in the recent fracture system of the inner shelf around Alboran
861 Island, Western Mediterranean. *Geo-Marine Letters*, *28*, 53–64.
862 https://doi.org/10.1007/s00367-007-0089-8

Martinez, F., & Taylor, B. (1996). Backarc spreading, rifting, and microplate rotation, between transform faults in the Manus Basin. *Marine Geophysical Researches*, *18*, 203–224. https://doi.org/10.1007/BF00286078

Martinez, F., & Taylor, B. (2003). Controls on back-arc crustal accretion: Insights from the Lau, Manus and Mariana basins. In R. D. Larter & P. T. Leat (Eds.). *Intra-Oceanic Subduction Systems: Tectonic and Magmatic Processes* (Vol. 219, pp. 19–54). London, UK: The Geological Society of London, Special Publications. https://doi.org/10.1144/GSL.SP.2003.219.01.02

Martinez, F., & Shipboard Scientific Party (2013). R/V Kilo Moana KM1129 [cruise data]. Available from *Rolling Deck to Repository (R2R)*: https://doi.org/ 10.7284/903698

Mallard, C., Coltice, N., Seton, M., Müller, R. D., & Tackley, P.J. (2016). Subduction controls the distribution and fragmentation of Earth's tectonic plates. *Nature*, *535*, 140–143. https://doi.org/10.1038/nature17992

Mann, P., Taylor, F. W., Edwards, R. L., Ku, T. -K. (1995). Actively evolving microplate formation by oblique collision and sideways motion along strike-slip faults: An example from the northeastern Caribbean plate margin. *Tectonophysics*, *246*, 1–69. https://doi.org/10.1016/0040-1951(94)00268-E

McKenzie, D. P. (1969). The relation between fault plane solutions for earthquakes and the directions of the principal stresses. *Bulletin of the Seismological Society of America*, *59*, 591–601.

Meffre, S., & Crawford, A. J. (2001). Collision tectonics in the New Hebrides arc (Vanuatu). *The Island Arc*, *10*, 33–50. https://doi.org/10.1046/j.1440-1738.2001.00292.x

885 Millen, D. W., & Hamburger, M. W. (1998). Seismological evidence for tearing of the Pacific
886 Plate at the northern termination of the Tonga subduction zone. *Geology*, *26*, 659–662.
887 https://doi.org/10.1130/0091-7613(1998)026<0659:SEFTOT>2.3.CO;2

888 Morley, C. K., Haranya, C., Phoosongsee, W., Pongwapee, S., Kornsawan, A., & Wonganan, N.
889 (2004). Activation of rift oblique and rift parallel pre-existing fabrics during extension and
890 their effect on deformation style: examples from the rifts of Thailand. *Journal of Structural*
891 *Geology*, *26*, 1803–1829. https://doi.org/10.1016/j.jsg.2004.02.014

892 Neves, M., Searle, R., & Bott, M. (2003). Easter microplate dynamics. *Journal of Geophysical*
893 *Research: Solid Earth*, *108*, 2213. https://doi.org/10.1029/2001JB000908

894 Nijholt, N., & Govers, R. (2015). The role of passive margins on the evolution of subduction-
895 transform edge propagators (STEPs). *Journal of Geophysical Research: Solid Earth*, *120*,
896 7203–7230. https://doi.org/10.1002/2015JB012202

897 Nilsson, K., Florendo, F., & Hawkins, J. W. (1989). Petrology of a nascent triple junction,
898 northeastern Lau Basin. *Eos*, *73*, 1389.

899 Park, J. -W., Campbell, I. H., Kim, J., Moon, J. -W. (2015). The role of late sulfide saturation in
900 the formation of a Cu- and Au-rich magma: Insights from the platinum group element
901 geochemistry of Niuatahi-Motutahi lavas, Tonga rear arc. *Journal of Petrology*, *56*, 59–81.
902 https://doi.org/10.1093/petrology/egu071

903 Parson, L., Pearce, J. A., Murton, B., & Hodkinson, R. (1990). Role of ridge jumps and ridge
904 propagation in the tectonic evolution of the Lau back-arc basin, southwest Pacific. *Geology*,
905 *18*, 470–473. https://doi.org/10.1130/0091-7613(1990)018<0470:RORJAR>2.3.CO;2

Pelletier, B., Lagabrielle, Y., Benoit, M., Cabioch, G., Calmant, S., & Garel, E. (2001). Newly identified segments of the Pacific-Australia plate boundary along the North Fiji transform zone. *Earth and Planetary Science Letters*, *193*, 347–358. https://doi.org/10.1016/S0012-821X(01)00522-2

Phillips, D. A. (2003). Crustal motion studies in the Southwest Pacific: Geodetic measurements of plate convergence in Tonga, Vanuatu and the Solomon Islands (Doctoral dissertation). Retrieved from ProQuest. (https://search.proquest.com/docview/305327521). Honolulu, HI: University of Hawai'i at Manoa.

Regelous, M., Turner, S., Falloon, T. J., Taylor, P., Gamble, J., & Green, T. (2008). Mantle dynamics and melting beneath Niuafo'ou Island and the northern Lau back-arc basin. *Contributions to Mineralogy and Petrology*, *156*, 103–118. https://doi.org/10.1007/s00410-007-0276-7

Resing, J., & Shipboard Scientific Party (2009). R/V Thomas G. Thompson TN234 [cruise data]. Available from *Rolling Deck to Repository (R2R)*: https://doi.org/ 10.7284/903993

Resing, J. A., Baker, E. T., Luption, J. E., Lilley, M. D., Rubin, K. H., & Buck, N. J. (2011a, December 5–9). *The Chemistry of Hydrothermal venting at a Volcano "O", a large Submarine Volcano in the NE Lau Basin*. Paper presented at the American Geophysical Union Fall Meeting 2011, San Francisco, CA. Abstract retrieved from https://ui.adsabs.harvard.edu/abs/2011AGUFM.V53D2652R/abstract

Resing, J. A., Rubin, K. H., Embley, R. W., Lupton, J. E., Baker, E. T., Dziak, R. P., Baumberger, T., Lilley, M. D., Huber, J. A., Shank, T. M. et al. (2011b). Active submarine

927 eruption of boninite in the northeastern Lau Basin. *Nature Geoscience*, *4*, 799–806.
928 https://doi.org/10.1038/ngeo1275

929 Rubin, K., & Shipboard Scientific Party (2010). R/V Kilo Moana KM1024 [cruise data].
930 Available from *Rolling Deck to Repository (R2R)*: https://doi.org/10.7284/900840

931 Rubin, K., & Embley, R. (2012). *Identification and implications of a submarine monogenetic*
932 *field in the NE Lau Basin*. Paper presented at the American Geophysical Union Fall Meeting
933 2012, San Francisco, CA. Abstract retrieved from
934 https://ui.adsabs.harvard.edu/abs/2012AGUFM.V44C..08R/abstract

935 Rubin, K., Embley, R., Arculus, R., & Lupton, J. (2013). *Magmatically greedy rear-arc*
936 *volcanoes of the N. Tofua segment of the Tonga arc*. Paper presented at the American
937 Geophysical Union Fall Meeting 2013, San Francisco, CA. Abstract retrieved from
938 https://ui.adsabs.harvard.edu/abs/2013AGUFM.V13I..04R/abstract

939 Rubin, K. H., & Embley, R. W. (2016). Tectonic and volcanic interplays in earths largest and
940 only known active boninite volcano province. *Geological Society of America Abstracts with*
941 *Programs*, *48*(7). https://doi.org/10.1130/abs/2016AM-286764.

942 Rubin, K., & Shipboard Scientific Party (2018). R/V Falkor FK171110 [cruise data]. Available
943 from *Rolling Deck to Repository (R2R)*: https://doi.org/10.7284/907642

944 Ruellan, E., Delteil, J., Wright, I., & Matsumoto, T. (2003). From rifting to active spreading in
945 the Lau Basin - Havre trough backarc system (SW Pacific): Locking/unlocking induced by
946 seamount chain subduction. *Geochemistry, Geophysics, Geosystems*, *4*, 8909.
947 https://doi.org/10.1029/2001GC000261

948 Scholz, C., & Campos, J. (1995). On the mechanism of seismic decoupling and back arc
949 spreading at subduction zones. *Journal of Geophysical Research: Solid Earth*, *100*, 22103–
950 22115. https://doi.org/10.1029/95JB01869

951 Schouten, H., Klitgord, K. D., & Gallo, D. G. (1993). Edge-driven microplate kinematics.
952 *Journal of Geophysical Research: Solid Earth*, *98*, 6689–6701.
953 https://doi.org/10.1029/92JB02749

954 Sdrolias, M., & Muller, R. D. (2006). Controls on back-arc basin formation. *Geochemistry,*
955 *Geophysics, Geosystems*, *7*, Q04016. https://doi.org/10.1029/2005GC001090

956 Sleeper, J. D. (2017). Tectonic and Magmatic Controls on Extension and Crustal accretion in
957 Backarc Basins, Insights from the Lau Basin and Southern Mariana Trough (Doctoral
958 dissertation). Retrieved from SOEST.
959 (https://www.soest.hawaii.edu/GG/academics/theses/Sleeper_Dissertation.pdf). Honolulu,
960 HI: University of Hawai'i at Manoa.

961 Sleeper, J. D., & Martinez, F. (2016). Geology and kinematics of the Niuafo'ou microplate in the
962 northern Lau Basin. *Journal of Geophysical Research: Solid Earth*, *121*, 4852–4875.
963 https://doi.org/10.1002/2016JB013051

964 Sleeper, J. D., Martinez, F., & Arculus, R. (2016). The Fonualei Rift and Spreading Center:
965 Effects of ultraslow spreading and arc proximity on back-arc crustal accretion. *Journal of*
966 *Geophysical Research: Solid Earth*, *121*, 4814–4835. https://doi.org/10.1002/2016JB013050

967 Stratford, W., Peirce, C., Paulatto, M., Funnell, M., Watts, A. B., Grevemeyer, I., & Bassett, D.
968 (2015). Seismic velocity structure and deformation due to the collision of the Louisville

969 Ridge with the Tonga-Kermadec Trench. *Geophysical Journal International*, *200*, 1503–
970 1522. https://doi.org/10.1093/gji/ggu475

971 Tappin, D., Bruns, T., & Geist, E. (1994). Rifting of the Tonga/Lau ridge and formation of the
972 Lau backarc basin: Evidence from site 840 on the Tonga Ridge. In J. Hawkins, L. Parson, J.
973 Allan, et al. (Eds.) *Proceedings of the Ocean Drilling Program, Scientific Results* (Vol. 135,
974 pp. 367–371). College Station, TX: Ocean Drilling Program.

975 Taylor, B., Zellmer, K., Martinez, F., & Goodliffe, A. (1996). Sea-floor spreading in the Lau
976 back-arc basin. *Earth and Planetary Science Letters*, *144*, 35–40.
977 https://doi.org/10.1016/0012-821X(96)00148-3

978 Taylor, P.W., & Ewart, A. (1997). The Tofua volcanic arc, Tonga, SW Pacific: Review of
979 historic volcanicactivity. Australian Volcanological Investigations (AVI) Occasional Report
980 No. 97/01. Pymble, New South Wales: Australian Volcanological Investigations.

981 Tian, L., Castillo, P. R., Hilton, D. R., Hawkins, J. W., Hanan, B. B., & Pietruszka, A. J. (2011).
982 Major and trace element and Sr-Nd isotope signatures of the northern Lau Basin lavas:
983 Implications for the composition and dynamics of the back-arc basin mantle. *Journal of*
984 *Geophysical Research: Solid Earth*, *116*, B11201. https://doi.org/10.1029/2011JB008791

985 Todd, E., Gill, J. B., Wysoczanski, R. J., Handler, M. R., Wright, I. C., & Gamble, J. A. (2010).
986 Sources of constructional cross-chain volcanism in the southern Havre Trough: New insights
987 from HFSE and REE concentration and isotope systematics. *Geochemistry, Geophysics,*
988 *Geosystems*, *11*, Q04009. https://doi.org/10.1029/2009GC002888

van Keken, P. E., Hacker, B. R., Syracuse, E. M., & Abers, G. A. (2011). Subduction factory: 4. Depth-dependent flux of H_2O from subducting slabs worldwide. *Journal of Geophysical Research: Solid Earth*, *116*, B01401. https://doi.org/10.1029/2010JB007922.

Wallace, L. M., Beavan, J., McCaffrey, R., & Darby, D. (2004). Subduction zone coupling and tectonic block rotations in the North Island, New Zealand. *Journal of Geophysical Research: Solid Earth*, *109*, B12406. https://doi.org/10.1029/2004JB003241

Wallace, L. M., McCaffrey, R., Beavan, J., Ellis, S. (2005). Rapid microplate rotations and backarc rifting at the transition between collision and subduction. *Geology*, *33*, 857–860. https://doi.org/10.1130/G21834.1

Wallace, L. M., Ellis, S., & Mann, P. (2009). Collisional model for rapid fore-arc block rotations, arc curvature, and episodic back-arc rifting in subduction settings. *Geochemistry, Geophysics, Geosystems*, *10*, Q05001. https://doi.org/10.1029/2008GC002220

Wiedicke, M., & Collier, J. (1993). Morphology of the Valu Fa spreading ridge in the southern Lau basin. *Journal of Geophysical Research: Solid Earth*, *98*, 11769–11782.

Wiedicke, M., & Habler, W. (1993). Morphotectonic characteristics of a propagating spreading system in the northern Lau Basin. *Journal of Geophysical Research: Solid Earth*, *98*, 11,783–11,797. https://doi.org/10.1029/93JB00707

Wysoczanski, R., Leonard, G., Gill, J., Wright, I., Calvert, A., McIntosh, W., Jicha, B., Gamble, J., Timm, C., Handler, M., Drewes-Todd, E., & Zohrab, A. (2019). Ar-Ar age constraints on the timing of Havre Trough opening and magmatism. *New Zealand Journal of Geology and Geophysics*, *62*, 371–377. https://doi.org/10.1080/00288306.2019.1602059

1010 Zellmer, K. E., & Taylor, B. (2001). A three-plate kinematic model for Lau Basin opening.
1011 *Geochemistry, Geophysics, Geosystems*, *2*. https://doi.org/10.1029/2000GC000106

1012 Zhang, H., Yan, Q., Li, C., Zhu, Z., Zhao, R., & Shi, X. (2018). Geochemistry of diverse lava
1013 types from the Lau Basin (SW Pacific): Implications for complex back-arc mantle dynamics.
1014 *Geological Journal*, *54*, 3643–3659. https://doi.org/10.1002/gj.3354